運輸省港湾技術研究所

港湾技術研究所報告

REPORT OF THE PORT AND HARBOUR RESEARCH INSTITUTE

MINISTRY OF TRANSPORT

VOL. 24 NO. 3 SEPT. 1985

NAGASE, YOKOSUKA, JAPAN

港湾技術研究所報告 (REPORT OF P.H.R.I.)

第24巻　第3号 (Vol. 24, No. 3), 1985年9月 (Sept. 1985)

目　　次 (CONTENTS)

REPORT OF THE PORT AND
HARBOUR RESEARCH INSTITUTE
Vol. 24, No. 3 (Sept. 1985)

2. Decay of Mechanically Generated Waves in an Opposing Wind

Hiroichi TSURUYA*
Shin-ichi YANAGISHIMA**
Yoshikuni MATSUNOBU**

Synopsis

An experimental study was conducted to measure the attenuation rates of mechanically generated regular and irregular water waves propagating against the wind. Measurements of static pressure and turbulence components in horizontal and vertical directions were also made with a disc probe and a X-type hot film probe. They were equipped to the servo-controlled wave follower.

Distribution of wind-driven current was measured and the group velocity of the waves propagating against this current was calculated. From the calculation it was confirmed that the group velocity of longer waves is not influenced very much by the wind-driven current.

From the measurements of the static pressure and turbulence components, the coupling coefficient was formulated in terms of the relative wind velocity and the wave slope. Correction factor of the coupling coefficient was estimated so that the attenuation coefficients of waves fit the measured data. Decay of component waves of irregular waves was also measured and it was confirmed that the attenuation of component waves can be estimated by the coupling coefficient obtained by the regular wave experiment.

Finally the diagrams which represent the decay of waves propagating against the wind were presented.

* Chief of Hydrodynamics Laboratory, Marine Hydrodynamics Division
** Member of Hydrodynamics Laboratory, Marine Hydrodynamics Division

港湾技術研究所報告
第24巻 第3号 (1985. 9)

2. 逆風による波の減衰に関する実験的研究

鶴谷 広一* ・柳嶋 慎一** ・松延 嘉國**

要 旨

逆風による波の減衰を調べるために，大型の風洞水路（幅1.5m，高さ1.3m，全長58.5m）を用いて実験的検討を行った。水路の一端にはブランジャー型の不規則波造波装置が設置され，風と逆方向に進行する波を発生させることができる。

実験には主として規則波が用いられたが，比較のために不規則波の減衰も調べられた。規則波の周期は2種類で，$T=1.111$ s と0.833 s であるが，これはそれぞれ0.9 Hz と1.2 Hz の波に相当する。それぞれの周期に対して波高は2種類（$T=1.111$ s の波に対しては$H=4.5$ cm と2.2 cm）の実験を行った。不規則波の有義波高は4.0 cm，有義波周期は1 s である。それぞれの波の条件に対して風速は主として5.2，6.6，7.9 m/s の3種類を与えた。

波の減衰の実験では測点に抵抗線式波高計を設置して，各ケースごとに水路中央と中央から±50 cm の合計3点で同一の測定をくり返し，フーリエ解析によって得られた規則波成分の波高のアンサンブル平均を求めた。

風と波のエネルギー交換を求めるために，風の吹出口から18.75mの地点に wave follower を取り付けて，波面から一定の高さにおける風の静圧と乱れ成分を同時に測定した。静圧の測定には disc 型プローブ，乱れの測定には水平と鉛直方向成分が同時に測れるX型のホットフィルム・プローブを用い，これらは wave follower に同一の高さに取り付けられた。

これらの測定値から逆風中での波と風のエネルギー交換を表す coupling coefficient μ を求める実験式を得た。このμを波の減衰係数に換算して，風洞内で実測された波の減衰係数と比較して，実測値により合うようにμの補正係数を求めた。

こうして求められた coupling coefficient から，いろいろな風速と波（周期，波形勾配）の条件における逆風中での波の減衰特性図を作成した。

* 海洋水理部 水理研究室長
** 海洋水理部 水理研究室

CONTENTS

1. Introduction

Recent port and coastal structures are apt to be constructed in deeper site than before. Moreover, the requests for the construction of offshore artificial islands and the development program of material resources in the ocean are increasing. In order to comply with these requests, it is necessary to predict the natural conditions accurately. In particular wave prediction is one of the most important procedures in planning and designing the offshore structures.

After the theoretical investigations of *Phillips* (1957) and *Miles* (1957) for the development of wind waves, many investigations have been made in the laboratory (*Shemdin and Hsu* 1967; *Mitsuyasu* 1968; *Wilson et al.* 1973; *Mizuno* 1975, 1976 a, 1978; *Mitsuyasu and Rikiishi* 1978; *Chao and Hsu* 1978; *Hsu et al.* 1981; *Mitsuyasu and Honda* 1982; *Plant* 1982; *Hsu and Hsu* 1983) as well as in the field (*Dobson* 1971; *Elliott* 1972; *Snyder* 1974; *Snyder et al.* 1981).

Compared to wave development, wave attenuation in an opposing wind has been paid little attention. And there is still a lack in the common understanding of this subject. A field measurement was undertaken by *Stewart and Teague* (1980), and some experimental studies have been made by *Mitsuyasu and Mizuno* (1971), *Mizuno and Mitsuyasu* (1973), *Mizuno* (1976 b), and *Young and Sobey* (1985). The last authors have measured the pressure and turbulence fluctuations of the wind over the waves propagating against the wind and estimated the coupling coefficient. However, they could not measure the wave attenuation with sufficient accuracy because of the limited length of their test flume. It now remains, consequently, to confirm that the coupling coefficient expresses the wave attenuation correctly.

In this experiment a long flume (the length of the measuring section is 28.5m) was used to measure the wave attenuation in an opposing wind with sufficient accuracy. Measurements of static pressure and turbulence of the wind were also made to obtain the coupling coefficient. The correction factor for the coupling coefficient was obtained to give a reasonable wave attenuation within the present experimental conditions.

2. Theoretical Background

2.1 Radiative Transfer Equation

Hasselmann (1968) has shown that for the constant depth of water, the radiative transfer equation for wave energy density can be represented as

$$\frac{\partial E(f,\theta;x,y,t)}{\partial t}+C_g\cos\theta\frac{\partial E(f,\theta;x,y,t)}{\partial x}+C_g\sin\theta\frac{\partial E(f,\theta;x,y,t)}{\partial y}=S, \quad (1)$$

where E is the directional spectral energy density of the component with the frequency f propagating toward the direction θ with the group velocity C_g; t is time, x and y are orthogonal coordinate directions, and S is a source function. The source function S represents the net transfer of energy to (or from) the spectrum at the frequency f due to all interaction processes. In determinig the source function S, three classes of source terms are considered: namely, direct influence of wind blowing over the waves S_a, nonlinear wave-wave interactions among components of the wave spectrum S_n, and dissipation such as wave breaking and bottom friction S_d. Thus,

$$S=S_a+S_n+S_d. \quad (2)$$

The energy flux S_a can be represented as

$$S_a=\alpha_a+\beta_a E(f,\theta), \tag{3}$$

where

$$\alpha_a(f,\theta)=\frac{2\pi^2\omega\Pi(k,\omega)}{\rho_w{}^2C^3C_g}, \tag{4}$$

represents the constant energy transfer to the wave field through turbulent atmospheric pressure fluctuations (*Phillips* (1957)), $\Pi(k,\omega)$ the wave number-frequency spectrum of the turbulent atmospheric pressure at the wave surface, ω the angular frequency, ρ_w the density of water, C the wave celerity, C_g the group velocity of the waves, and

$$\beta_a(f,\theta)=\mu\omega, \tag{5}$$

where μ is the coupling coefficient as originally formulated by *Miles* (1957). The coupling coefficient will be discussed later in this chapter.

The term S_n represents the energy transfer due to nonlinear wave-wave interactions and has the form

$$S_n=\int[T_1F(K')F(K'')F(K-K'-K'')-T_2F(K)F(K')F(K'')]dK'dK'', \tag{6}$$

where F is the energy spectrum in terms of wave number, T_1 and T_2 are complicated coupling coefficients and are given by *Hasselmann* (1963). If the frequencies of swell and wind-generated waves are sufficiently separated, there is little interaction between the two. Consequently, the term S_n is neglected in the present study.

The term S_d cannot be easily determined because it contains such highly indistinct processes as weve-breaking and percolation. The dissipation in shallow water can be formulated by making use of the theory by *Hunt* (1952) for viscous dissipation or that of turbulent bottom friction based on a quadratic friction law by *Hasselmann and Collins* (1968).

2.2 Potential Theory of Air Flow over Water Waves

Instability of two superposed inviscid fluids with the densities ρ and ρ' one beneath the other, moving parallel to x direction with velocities U, U' is considered after the treatment by *Lamb* (1932).

If the effect of viscosity of the fluids are neglected and the perturbed flow is assumed to be irrotational, the velocity potential ϕ can be introduced so that

$$u=-\frac{\partial\phi}{\partial x}, \tag{7}$$

$$w=-\frac{\partial\phi}{\partial z}, \tag{8}$$

where x and z are the horizontal and vertical coordinates, and u and w, horizontal and vertical velocities, respectively. It is assumed that only the upper fluid is moving with a uniform mean velocity U.

The velocity potential ϕ for the upper liquid can be written as

$$\phi=-Ux+\phi_1, \tag{9}$$

where ϕ_1 is small by hypothesis.

For the water surface elevation

$$\eta=ae^{i(\omega t-kx)}, \tag{10}$$

where a is the amplitude of waves, ϕ_1 can be represented as

$$\phi_1=C_pe^{-kz+i(\omega t-kx)}, \tag{11}$$

where C_p is a constant.

The kinematic free surface boundary condition is

$$\frac{\partial \eta}{\partial t}+U\frac{\partial \eta}{\partial x}=-\frac{\partial \phi}{\partial z}. \tag{12}$$

Substitution of Eqs. (10) and (11) into (12) yields

$$C_p=ia(C-U), \tag{13}$$

where C is the phase velocity of the waves. The velocity potential is, then,

$$\phi=-Ux+ia(C-U)\exp\{-kz+i(\omega t-kx)\}. \tag{14}$$

The horizontal and vertical velocity components can be written from Eqs. (7), (8) and (14), namely,

$$\frac{u}{C}=\frac{U}{C}-ka\left(1-\frac{U}{C}\right)e^{-kz}\cos(\omega t-kx), \tag{15}$$

and

$$\frac{w}{C}=ka\left(1-\frac{U}{C}\right)e^{-kz}\cos\left(\omega t-kx+\frac{\pi}{2}\right). \tag{16}$$

The air pressure is obtained from *Bernoulli's* equation for unsteady irrotational motion (e.g., see *Young* 1983) and the result can be written as

$$\frac{p}{\rho_a g}=-ae^{-kz}\left(1-\frac{U}{C}\right)^2\cos(\omega t-kx)-z. \tag{17}$$

Notice that the air pressure is always 180° out of phase with the water surface. The horizontal velocity component u, on the other hand, is 180° out of phase only when $U/C<1$. In the case of an opposing wind, U/C is negative so that the u component is always 180° out of phase with the water surface.

2.3 Coupling Coefficients

A theory for deep water waves has been well established by *Young* (1983) for the coupling coefficients for the air-water energy flux in the orthogonal curvilinear system on the water surface. The development below follows his work.

For the motion of water surface defined by

$$\eta=a\cos(kx-\omega t), \tag{18}$$

the effective normal stress at the water surface can be written as

$$\tilde{\sigma}_e=(\nu+i\mu)\rho_w C^2 k\eta, \tag{19}$$

where ν and μ are the coupling coefficients which are in practice both small, ρ_w the density of water and the tilde on $\tilde{\sigma}_e$ indicates a wave-induced quantity with frequency ω.

The energy flux caused by the working of the effective normal stress is

$$\frac{\partial E}{\partial t}=\overline{\tilde{\sigma}_e\frac{\partial \eta}{\partial t}}. \tag{20}$$

From Eqs. (18), (19) and (20) the energy flux can be written as

$$\frac{\partial E}{\partial t}=\mu\omega E, \tag{21}$$

where the coupling coefficient μ determines the rate of the air-water energy flux. In

tensor notation, the momentum equation is

$$\rho_a\left\{\frac{\partial u_i}{\partial t}+\frac{\partial}{\partial x_j}(u_i u_j)\right\}=\rho_a g_i+\frac{\partial \sigma_{ij}}{\partial x_j}, \tag{22}$$

where $u_i(x_i, t)$ is the instantaneous velocity in the x_i direction and $\sigma_{ij}(x_i, t)$ is the instantaneous stress tensor. The pressure $p(x_i, t)$ can be expressed as

$$p=\overline{p}+\tilde{p}+p', \tag{23}$$

where the upper bar denoting the overall time average, the tilde indicates a wave-induced pressure with frequency ω and the prime indicates the uncorrelated turbulent residual. The velocities can be represented in a similar manner :

$$u_i=\bar{u}_i+\tilde{u}_i+u_i', \tag{24}$$

with a decomposition as in Eq. (23).

Substitution of Eq. (24) into Eq. (22) and time-averaging yields

$$\rho_a\left\{\frac{\partial \bar{u}_i}{\partial t}+\frac{\partial}{\partial x_j}(\bar{u}_i \bar{u}_j)\right\}=\rho_a g_i+\frac{\partial}{\partial x_j}\left(\sigma_{ij}-\rho_a\overline{\tilde{u}_i\tilde{u}_j}-\rho_a\overline{u_i' u_j'}\right), \tag{25}$$

where the third and the fourth terms in the right-hand side are the wave-induced and turbulent Reynolds stresses, respectively.

These stress components may cause an energy flux to (or from) the waves. This flux is proportional to the component of stress in phase with the wave slope for normal stresses or in phase with the water surface for a tangential stress (*Longuet-Higgins* (1969)).

Laboratory measurements of stress components are generally made in a rectangular cartesian coordinate system. The water surface is oscillatory and the effective stress component to the energy flux would act in the direction normal to the water surface. Consequently, measured stress components must be transformed into the orthogonal curvilinear system in the water surface. *Young* (1983) has obtained the expression for the coupling coefficient μ for the orthogonal curvilinear system in the water surface as

$$\begin{aligned}\mu=\Big\{&-\mathrm{amp}(\tilde{p})\sin\phi_{\tilde{p}\tilde{\eta}}-\mathrm{amp}\left(\frac{\partial\eta}{\partial x}\right)\rho_a\overline{(\tilde{u}+u')^2}\\&-\mathrm{amp}\left(\frac{\partial\eta}{\partial x}\right)\rho_a(\tilde{u}+u')(\tilde{w}+w')+\mathrm{amp}\left(\frac{\partial\eta}{\partial x}\right)2\mu_a\frac{\partial\overline{u}}{\partial x}\\&+\mathrm{amp}\left(\frac{\partial\eta}{\partial x}\right)\mu_a\left(\frac{\partial\overline{w}}{\partial x}+\frac{\partial\overline{u}}{\partial z}\right)\Big\}/\rho_w C^2 ak,\end{aligned} \tag{26}$$

where $\phi_{\tilde{p}\tilde{\eta}}$ is the phase difference between $\tilde{p}$ and $\tilde{\eta}$, μ_a the dynamic viscosity of air, ρ_w the density of water and amp( ) indicates the amplitude of the quantity in brackets. The first term in the right-hand side of Eq. (26) represents the contribution due to normal stress, the second and third terms represent the effects of Reynolds stresses, while the final two terms are viscous stress contributions.

3. Experimental Facility and Instrumentation

3.1 Experimental Facility

The experiments were conducted in a wind-wave tunnel, whose sketches are given in Figs. 1(a) and 1(b). The dimensions of the test section are 2,850cm long, 150cm wide and 130cm deep. A wind blower is located on the windward side of the test section over

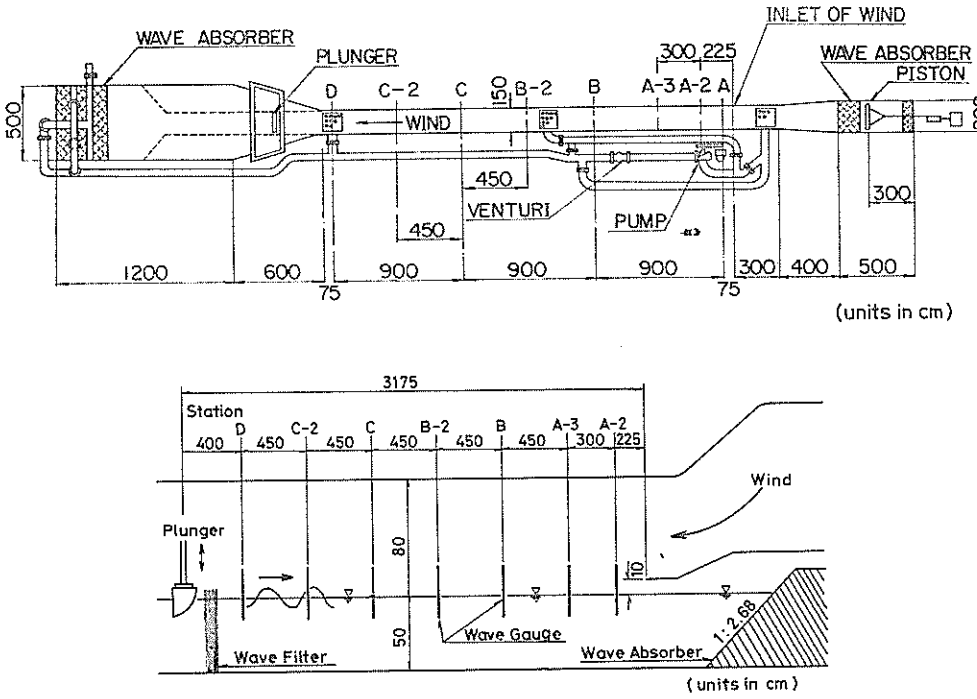

Fig. 1 Wind-wave Tunnel

the waterway, and wind is generated by an axial fan driven by a 50kW variable speed motor. The wind tunnel is fitted with guide vanes, a fine mesh screen, and honeycombs in order to provide uniform velocity profiles. The wind is introduced in the tunnel by a guide plate which is horizontally fixed 10cm above the water surface. The height of the clearance was so set that the mechanically generated waves could proceed without any obstructions.

A mesh wave absorber in which small plastic films are installed is located under the guide plate.

On the leeward of the uniform test section, an enlarged part is fitted in order to diffuse winds. In this part, a plunger-type irregular wave maker is installed. This plunger is controlled by a low-inertia DC motor (0.77 kW), the movement of which is directly proportional to the input signal supplied from the controlling instruments such as the synthesized function generator or the analog data recorder. In the regular wave experiments the synthesized function generator was used in order to generate the sinusoidal signal. Wave period is adjusted by setting the 4-digit figure dials. In the irregular wave experiments, the wave signal having the shape of *Bretschneider-Mitsuyasu* spectrum was computed by ACOS 1000/10 digital computer system of the Port and Harbour Research Institute. The result was recorded on a magnetic tape in a digital form. This digital data was transformed by the D-A converter (DATAC-2000 B, Iwatsu Electronic Co., Ltd.) into analog data with the time intervals of 1/128 s and was recorded on a cassete type data recorder (R-61, TEAC Corp.). At every experiment concerning irregular waves, this analog data recorder was used to supply a wave signal to the irregular wave controller. The maximum amplitude of the plunger movement can be easily established by setting the 3-digit figure dials. Wave filters of stainless wire gauzes were installed ahead of the plunger to prevent reflection of wind waves.

3. 2 Instrumentation

Measurements of waves were made simultaneously at seven locations with resistance-type wave gauges. The senser consists of two parallel platinum wires of 0. 1 mm diameter. Spacing of the wires is 2 mm.

Mean wind velocities were measured with a Pitot-static tube and a MKS BARATRON type 310BH differential pressure head and type 170 M-6 B electronic unit.

The fluctuating wind velocities in horizontal and vertical directions were measured with a DISA 55 R 61 hot-film probe, 55 M 01 anemometers and 55 M 25 linearizers.

The static pressure was measured with a brass disc probe, 8 mm in diameter with a thickness of 1. 5 mm.

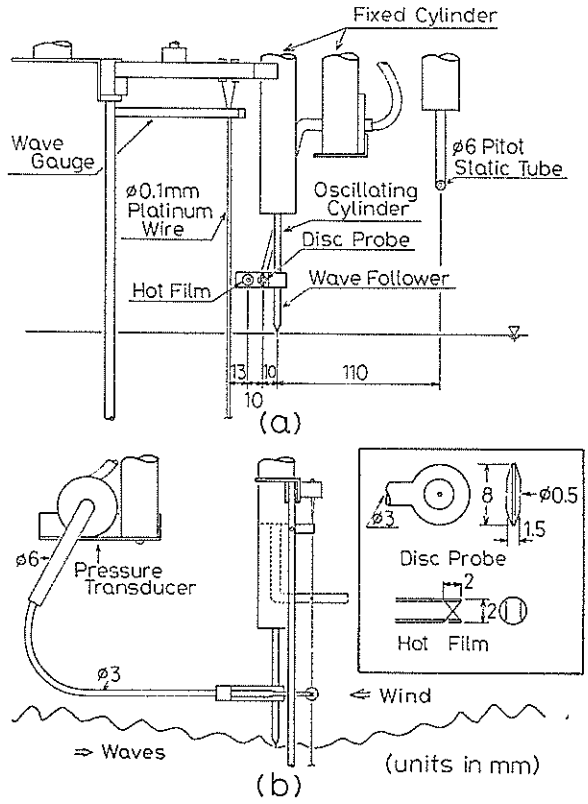

Fig. 2 Arrangement of Sensors

The arrangement of the sensors is shown in Fig. 2. The disc probe is connected to the pressure transducer (DP 4 X-20, Sankei Engineering Co., Ltd.) through a vinyl chloride pipe 30 cm in length and 3 mm in diameter. The measurement range of the pressure transducer is from zero to 20 mm H_2O. The distance between the disc probe and the hot-film probe is 10 mm. The platinum wires of the wave gauge is located 13 mm apart from the hot-film probe in the plane normal to the wind direction including the disc and hot-film probes. The hot-film probe and disc probe were mounted on a wave follower, which was located at the distance 25 mm ahead of the wave gauge and with the lateral spacing 33 mm from the latter. The wave follower has a water content platinum needle, the submergence length of which is servo-controlled with the response time of 2. 5 ms/mm. This response speed is equivalent to the velocity of 40 cm/s. An example of the

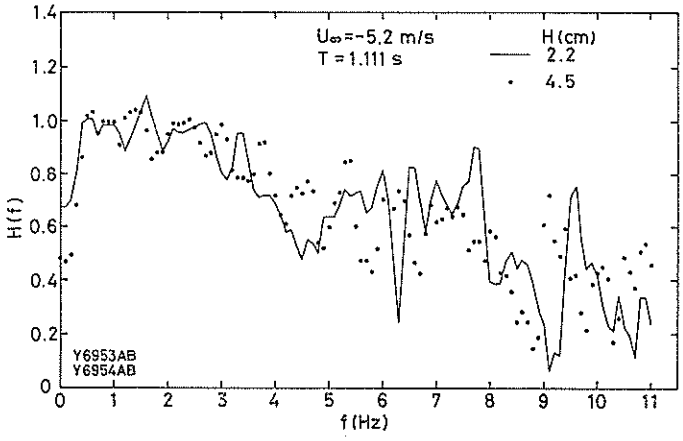

Fig. 3 Response Function of Wave Follower

response function $H(f)$ of the wave follower movement to the signal of the resistance-type wave gauge is illustrated in Fig. 3. The period of the mechanically generated waves is 1.111 s ($f=0.9$ Hz) and the peak frequency of wind waves is 2.5 Hz. Some fluctuations can be recognized in the frequency range from $f=1.0$ Hz to 2.0 Hz in Fig. 3. However, the spectral density in this range is very small compared with those of the mechanically generated waves and wind waves, and therefore the accuracy in estimating the response function in this frequency range is not high. Consequently, we regard that the response characteristics of the wave follower has no problem up to the peak frequency of wind waves, say $f=2.5$ Hz.

The elevation of the disc probe and the hot-film probe above the water surface was adjusted by setting their supporting frame of the wave follower at a designated height. The elevation was selected between the range from 2.5 to 11 cm during measurements.

4. Experimental Procedures

In this experiment, regular waves were mainly used in order to measure the wave

Table 1 Experimental Conditions

	T(s)	H(cm)	L(m)	C(m/s)	H/L	U_∞(m/s)	U_∞/C
regular waves	1.111	2.2	1.81	1.63	0.012	− 5.2	−3.19
						− 6.6	−4.05
		4.5			0.025	− 7.9	−4.85
						−10.8	−6.63
	0.833	2.7	1.08	1.29	0.025	− 5.2	−4.03
						− 6.6	−5.12
		4.4			0.041	− 7.9	−6.12
irregular waves	1.0*	4.0**	1.51	1.51	0.026	− 5.2	−3.44
						− 6.6	−4.37
						− 7.9	−5.23

* significant wave period
** significant wave height

decay, and the wind pressure and turbulence. Irregular waves were also used for comparison. The experimental conditions are summerized in Table 1.

The pitot-static tube was vertically traversed from the point close to the moving water surface to the elevation 70 cm above the surface. The friction velocity u_{*a} was estimated by applying the logarithmic law to the measured wind velocity profile near the water surface. The maximum wind velocity in the tunnel was determined as the free-stream wind velocity U_∞ which appeared near the center of the wind passage ($z=40\sim50$ cm).

In the case of $T=1.111$ s, measurements of surface elevations were made at 7 stations A-2, A-3, B, B-2, C, C-2 and D as shown in Fig. 1. In the case of $T=0.833$ s, measurements were made from station D to C, because when wind was blowing the waves were likely to be unstable between stations B-2 and A-2.

Procedures in measuring the waves in an opposing wind are as follows. First, the gates just before the fan is closed. When the rotational speed of the fan reaches to the setting value, the gates are slowly opened. One minute after the start of wind, the plunger located at the distance 32 m from the inlet of wind begins to generate waves. Fifty seconds after the generation of waves, wave data are recorded on-line to the digital data recorder (DATAC-2000 B, Iwatsu Electronic Co., Ltd.).

The group velocity C_g of the regular waves of $T=1.111$ s is 0.99 m/s if the wind effect is ignored. The time T_E that the wave energy reaches the inlet of wind is calculated as

$$T_E=32/0.99=32.3 \text{ (s)}. \tag{27}$$

In general, the group velocity is slightly decreased by a wind-driven current in a test flume. The rate of decrease in the group velocity for the present regular waves ($T=1.111$ s) is estimated as less than 2% as will be discussed in 6.2. Consequently, it can be considered that the time interval fifty seconds between the start of mechanically generated waves and the commencement of recording is sufficiently long for mechanically generated waves to reach the equilibrium condition of decay by the wind. In the case of $T=0.833$ s, it can be easily confirmed that the time interval fifty seconds is also sufficient because the measurement of waves were made between stations D and C. In the case of irregular waves with the significant wave period $T_{1/3}=1$ s, energy of the component waves $0<f<1.16$ Hz can reach the inlet of wind in fifty seconds if the wind effect is neglected. Within this frequency range, 70% of the total energy is contained. Energy of the frequency component $f=1.4$ Hz which will be cited in Fig. 26 can reach the inlet of wind in 57.2 s if the wind effect is neglected, but the beginnig of the wave recording was set at 50 s after the start of wind to keep the experimental condition constant.

All the wave data were measured at the center of each station and ±50 cm apart from the center line of each station. Therefore, three sets of measurements in one experimental condition were taken and the calculated results were averaged to yield the ensemble mean. Measurements of static pressures and turbulence of winds were made at station C, making use of the wave follower in order to maintain the measuring height constant from the moving water surface.

The disc probe compresses the adjacent streamlines and the measured data indicate a slightly smaller value than the true static pressure (*Young* 1983). The pressure recorded by the disc p_d can be represented as

$$p_d=p_s-\frac{1}{2}K\rho_a{}^2U^2, \tag{28}$$

where p_s is the static pressure, U the wind velocity, ρ_a the density of air, and K is a constant which has been determined by calibration. The relation between the amplitudes

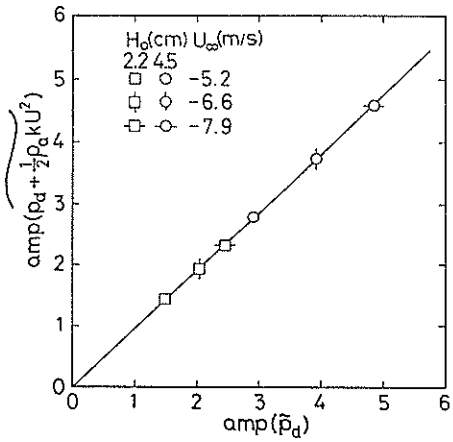

Fig. 4 Relationship between the Raw and Corrected Values of the Wave-Induced Pressure

of the disc pressure p_d and the corrected pressure by the wind velocity is shown in Fig. 4. The straight line shows the relation

$$\text{amp}\left(\overline{p_d+\frac{1}{2}K\rho_a U^2}\right)=0.943\ \text{amp}(\tilde{p}_d), \tag{29}$$

where $K=0.06303$. There exists a difference of 5.7% between the raw and corrected pressure. The above relation indicates that the static pressure p_s can be estimated by the disc pressure p_d without analysis of the wind velocity U, even though a correction by a fachor of 0.943 needs to be multiplied to p_d. The correction was made at the final stage of analysis in this study, and all the pressure data are shown with the value p_d in this report.

In the measurement of waves, the sampling time interval was $\Delta t=1/51.2$ s, the total data number at one station was $N=8192$, and the duration time of one measurement was 160 s. In the measurement of wind pressure and turbulence, on the other hand, $\Delta t=1/102.4$ s and $N=16384$. The water depth was kept constant at 50 cm throughout the experiment.

5. Data Analysis

An instantaneous signal $g(t)$, for example, wind velocity of turbulent air stream or a static air pressure disturbed by water waves, can be decomposed into three different components:

$$g(t)=\bar{g}+\tilde{g}(t)+g'(t), \tag{30}$$

where $\bar{g}$ is the time-independent mean component, $\tilde{g}(t)$ the wave-induced quantity, and $g'(t)$ the uncorrelated turbulent residual.

The time average which yields the mean value of $g(t)$ is defined as

$$\bar{g}=\lim_{T_0\to\infty}\frac{1}{T_0}\int_0^{T_0} g(t)dt, \tag{31}$$

where T_0 is the duration time of measurement.

The wave-induced component can be obtained by making use of the Fourier analysis. Periods of mechanically generated waves used in this experiment are 1.111 s and 0.833 s. Frequencies of these waves are 0.9 Hz and 1.2 Hz exactly. The Fourier components corresponding to these wave frequencies can be easily obtained by using the FFT algorithm. The signal may be expanded into a Fourier series according to the following formula (*Bendat and Piersol* 1966)

$$g(t)=\frac{a_0}{2}+\sum_{n=1}^{\infty}(a_n\cos 2\pi nf_1t+b_n\sin 2\pi nf_1t),$$

where

$$f_1=\frac{1}{T_0}, \tag{32}$$

$$a_n=\frac{2}{T_0}\int_0^{T_0} g(t)\cos 2\pi n f_1 t\,dt,\quad n=0,1,2,\cdots\cdots,$$

$$b_n=\frac{2}{T_0}\int_0^{T_0} g(t)\sin 2\pi n f_1 t\,dt,\quad n=1,2,3,\cdots\cdots.$$

The fundamental frequency f_1 for the measurement time $T_0=160$ s is $f_1=1/T_0=0.00625$ Hz so that the wave frequencies for $f=0.9$ and 1.2 Hz correspond to the 145-th and 193-rd Fourier components, respectively. The wave amplitude A_n of the n-th component is expressed with a_n and b_n in Eq. (32) as

$$A_n=\sqrt{a_n^2+b_n^2}. \tag{33}$$

In practice, the energy of wave-induced component may spread to the neighbouring frequencies to some extent, so that the frequency components with the range of ± 0.2 Hz from the central peak of the regular waves were considered as the part of wave-induced component. All the Fourier components within this frequency range were added together energetically by making use of Eq. (33). Increase in the synthesized amplitude over the amplitude of the central peak component was less than 2% for the case of pressure data. The turbulence component is then obtained by Eq. (30). It was confirmed that the correlations between the wave-induced and the turbulence components of wind velocity are negligibly small.

6. Experimental Results

6.1 Outline of the Results

Photo 1 and 2 show the situations in which an opposing wind is blowing over the mechanically generated waves at various wind speeds. The direction of the wind is from the right to the left and that of the mechanically generated waves is opposite.

Photo 1 was taken at the station A-2. As the fetch of this station is very short (F =2.25 m), wind waves do not grow sufficiently, but it would be easily recognized from

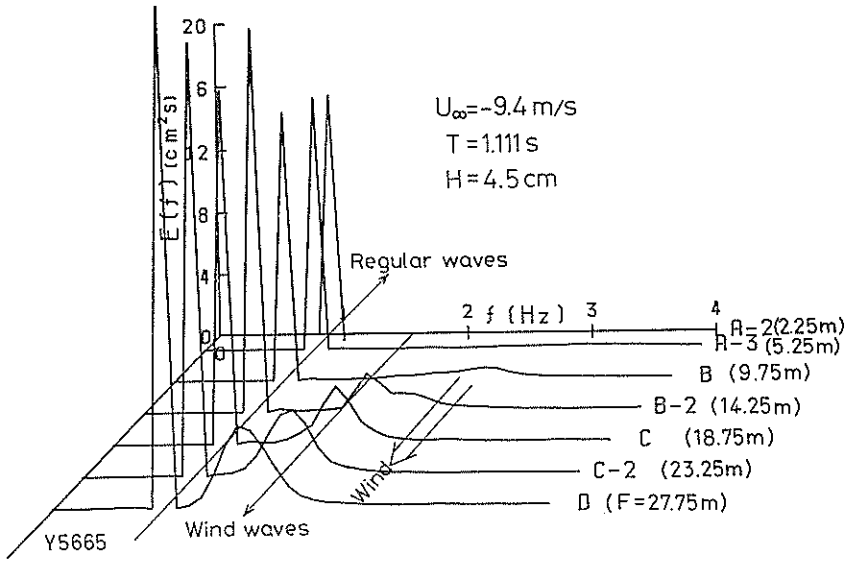

Fig. 5 Development of Wave Spectra with Fetch

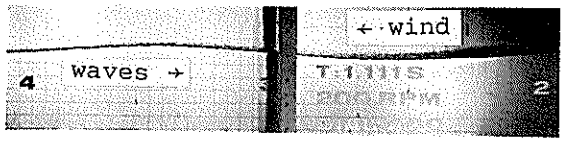

U_∞ (m/s)

−5.2

−6.6

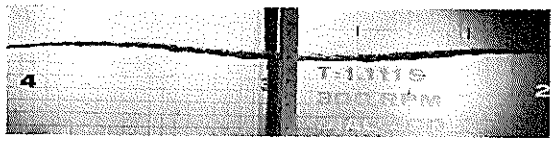

−7.9

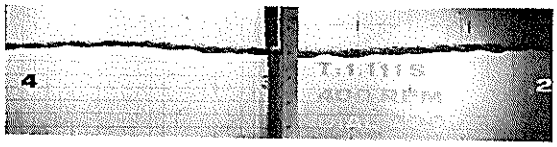

−10.8

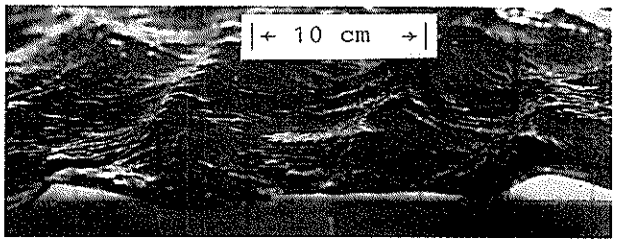

−10.8

(F≒3 m)

Photo 1 Waves Propagating in an Opposing Wind (Station A-2, H=4.5cm, T=1.111s)

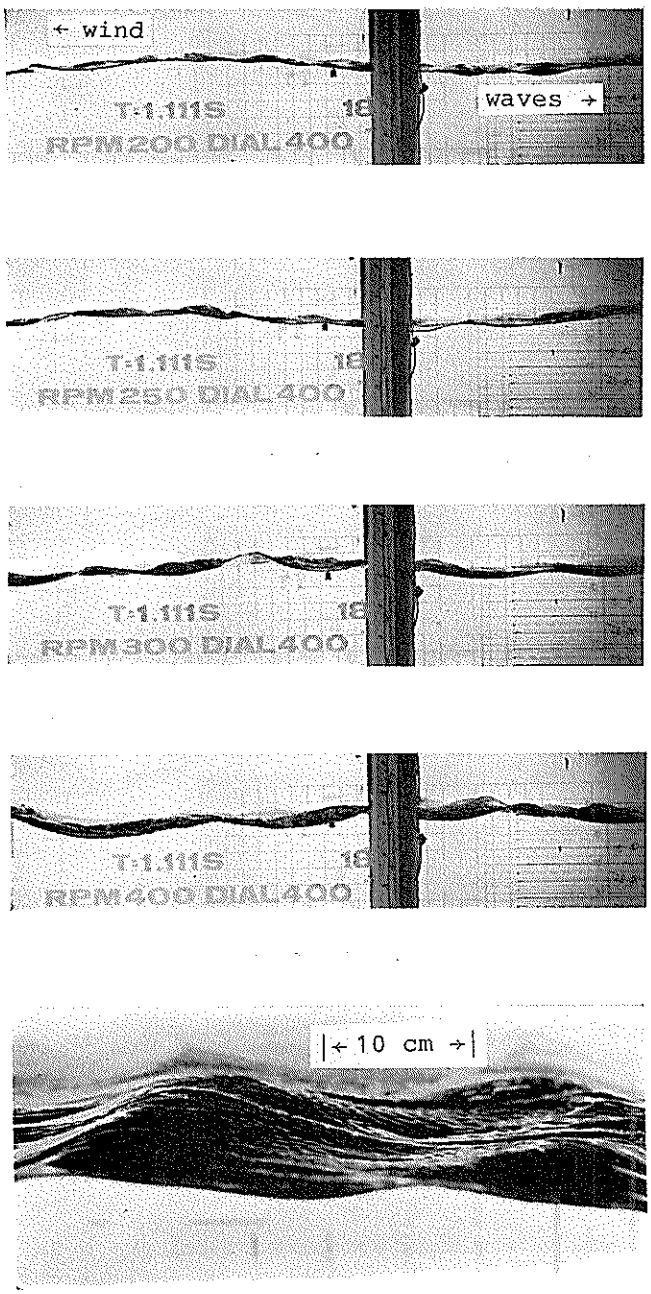

U_∞ (m/s)

−5.2

−6.6

−7.9

−10.8

−6.6

($F \fallingdotseq 18$ m)

Photo 2 Waves Propagating in an Opposing Wind (Station C, $H=4.5$cm, $T=1.111$s)

the photo that the height of mechanically generated waves are much reduced for higher wind speeds. The wave slope of wind waves riding on the swell is very steep as can be seen in the lowest frame. Photo 2 was taken at the station C. Growth of wind waves is remarkable compared with that of the station A-2.

An example of the development of frequeucy spectra of surface elevations with fetch is shown in Fig. 5. Wind waves grow as the fetch F increases and the peak frequency shifts to the lower frequencies. The sharp peak corresponds to the regular waves propagating against the wind. Although the peaks show some scatter in magnitude, the power decreases on the average as the regular waves proceed against the wind.

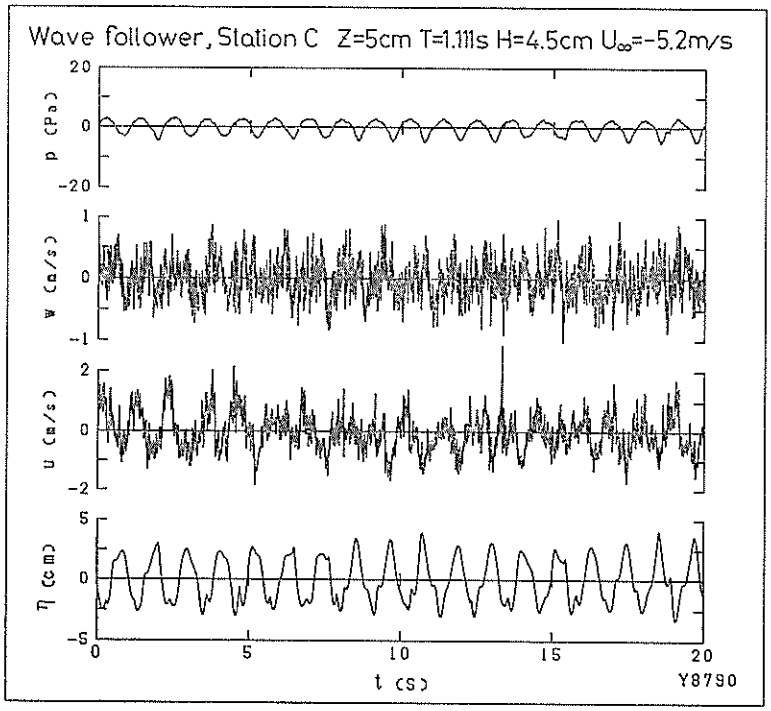

Fig. 6 Time Series of Surface Elevation η, Static Pressure p, and Turbulence Components u and w (wave following coordinate system)

Figure 6 shows the time variation of the surface elevation η, static pressure p, and wind turbulence components u and w in the horizontal x and vertical z directions, respectively. Static pressure was measured with the disc probe and turbulence components were measured with the hot-film anemometers. These probes were held at the height 5 cm above the moving water surface by means of the wave follower.

Both the static pressure p and the horizontal wind velocity fluctuations are nearly 180° out of phase with the surface elevation η as can be predicted by the potential theory, which has already been described in Section 2.2. Notice that the direction of the u component has been taken positive to the direction of the wave propagation. The ordinate of the w component was magnified two times larger than that of the u component. The turbulence level of the w component is smaller than that of the u component and it can be recognized that the phase is shifted about 90° with the water surface as predicted by Eq. (16). For comparison, similar data measured at a fixed elevation $z=5$ cm are

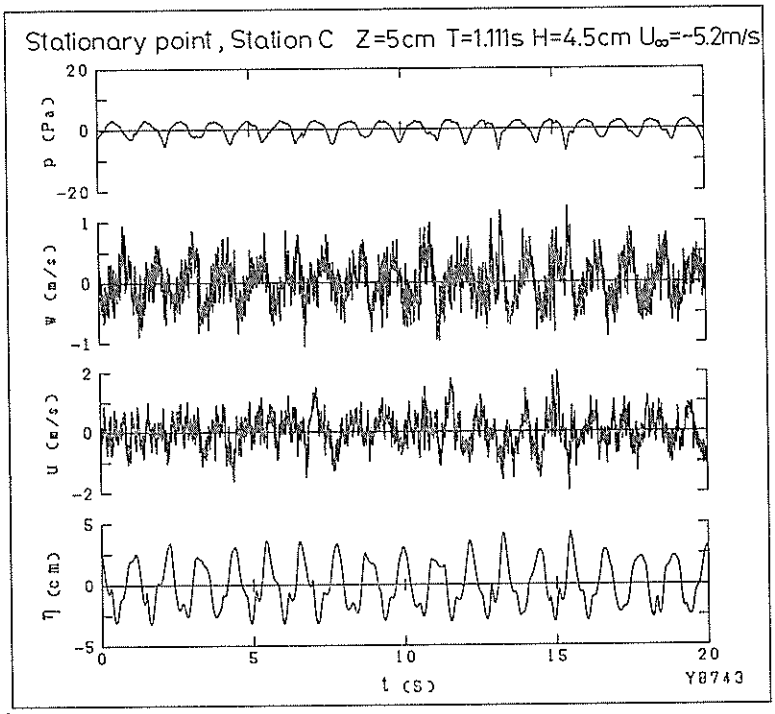

Fig. 7 Time Series of Surface Elevation η, Static Pressure p, and Turbulence Components u and w (stationary coordinate system)

illustrated in Fig. 7. There is a distinct phase lag of 90° between the w component (in advance) and the water surface, which is not clear in Fig. 6.

6.2 Drift Current and Group Velocity

(1) Drift Current Distribution

When wind blows over the water surface, wind-induced drift current is produced mainly by a surface shear stress. In general, currents have direct effects upon the wave speed and group velocity. *Mizuno and Mitsuyasu*(1973) have investigated the effects of adverse wind on the phase velocity of mechanically generated waves. In their study, influence of the wave-induced aerodynamic pressure was examined in addition to that of the drift current. Within their experimental conditions, the effect of drift current was greater than that of the aerodynamic pressure. As the wave period increases, however, the role of the aerodynamic pressure accounting for the change in the phase velocity increases.

For the case of following wind, *Kato et al.* (1976) have demonstrated that the effect of aerodynamic pressure on the phase speed is considerably small compared with that of the logarithmic drift current in the experimental wind-wave scales (L <60 cm).

In considering the wave attenuation (or growth), it will be necessary to examine the effects of drift current on the phase velocity and the group velocity of waves, because they are important factors in the calculation of the energy transfer or coupling coefficient by using Eqs. (1) and (26).

The effect of the aerodynamic pressure on the group velocity is difficult to examine, because the change of the phase speed by the aerodynamic pressure is obtainable only numerically but not analytically. And in the experimental scale the effect of the drift

current will be greater than that of the aerodynamic pressure as demonstrated by *Mizuno and Mitsuyasu* (1973) and *Kato et al.* (1976). In this study, therefore, only the effect of drift current is examined.

Figure 8 shows the vertical distribution of drift currents measured at the station C by making use of the Laser-Doppler Anemometer (LDA, DANTEC 55 X system). In order to investigate the group velocity, the logarithmic distribution is used, namely,

$$U_w(z)=u_0-U_r \ln\left(\frac{z_0-z}{z_0}\right)-bz, \tag{34}$$

where u_0 is the surface velocity, z_0 the roughness height, and U_r and b are the constants. The fitted curves and estimated constants are illustrated in Fig 8.

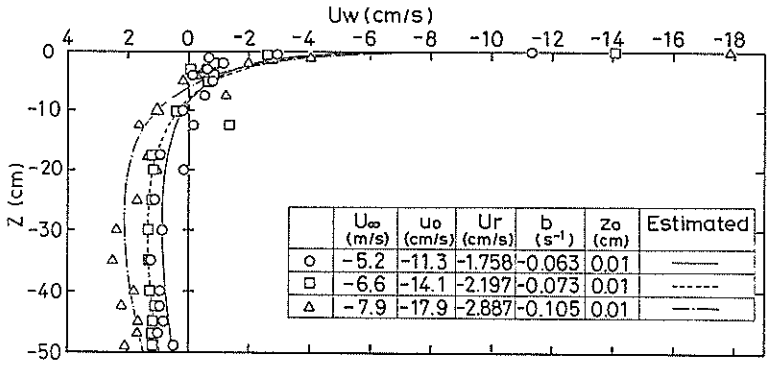

	U_∞ (m/s)	u_0 (cm/s)	U_r (cm/s)	b (s^{-1})	z_0 (cm)	Estimated
○	-5.2	-11.3	-1.758	-0.063	0.01	——
□	-6.6	-14.1	-2.197	-0.073	0.01	------
△	-7.9	-17.9	-2.887	-0.105	0.01	—·—

Fig. 8 Vertical Distribution of Drift Currents

(2) Calculation of Group Velocity in a Logarithmic Drift Current

Kato (1974) has shown that for a logarithmic drift current represented by Eq. (34) the phase speed of waves can be calculated by solving the linearized equations of motion by making use of the perturbation method. He has obtained up to the second order solution. For practical purposes, however, the first order solution is enough in calculating the phase speed.

The phase speed C can be expanded with a parameter $\varepsilon=u_0/C_0$ (C_0 is the phase speed in still water) as

$$C=C_0+\varepsilon C_1+\varepsilon^2 C_2+\cdots\cdots. \tag{35}$$

The first order solution can be written as

$$\frac{C_1}{C_0}=1+\frac{U_r}{u_0}\left(\frac{Q}{2k\sinh 2kh}-\frac{\delta}{2kz_0}\tanh kh\right), \tag{36}$$

where

$$Q=2k\left[\frac{\cosh 2kh}{y_1}-\frac{1}{y_1}+\sinh y_2(\mathrm{Chi}\, y_1-\mathrm{Chi}\, y_2)\right.$$
$$\left.+\cosh y_2(\mathrm{Shi}\, y_2-\mathrm{Shi}\, y_1)\right]-\frac{d}{z_0(d+z_0)}, \tag{37}$$

$$\delta=1-z_0 b/U_r, \tag{38}$$

$$y_1=2kz_0, \tag{39}$$

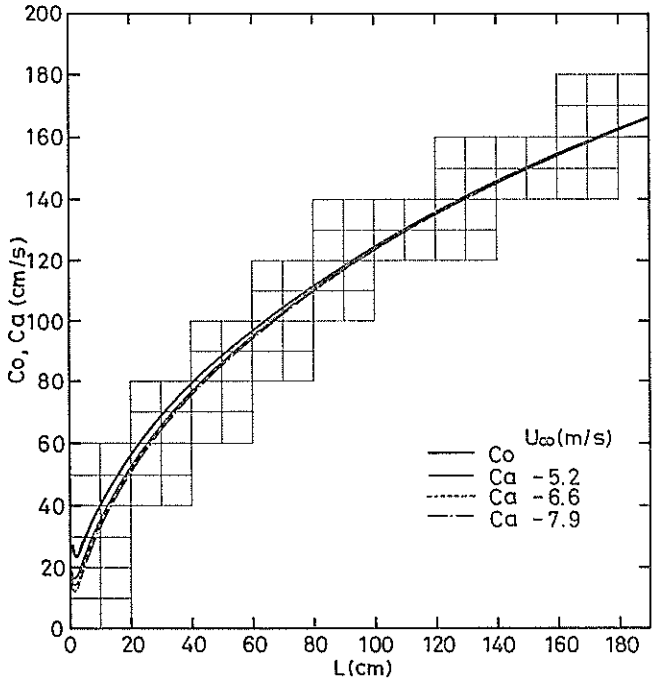

Fig. 9 Phase Velocity C_0 in Still Water and C_a Propagating Against the Drift Current

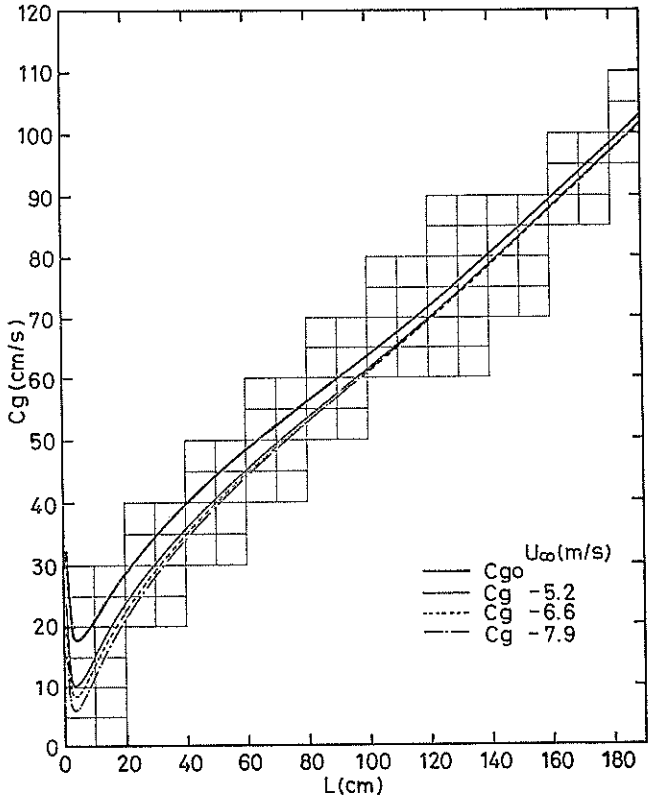

Fig. 10 Group Velocity C_{g0} in Still Water and C_g Propagating Against the Drift Current

$$y_2=2k(h+z_0), \tag{40}$$

$$\left.\begin{aligned}&\text{Shi } x=x+\frac{x^3}{3\cdot 3!}+\frac{x^5}{5\cdot 5!}+\cdots\cdots,\\&\text{Chi } x=\ln|x|+\frac{x^2}{2\cdot 2!}+\frac{x^4}{4\cdot 4!}+\cdots\cdots.\end{aligned}\right\} \tag{41}$$

The group velocity is then given by

$$C_g=\frac{d\omega}{dk}=\frac{d}{dk}(kC). \tag{42}$$

Figure 9 shows the phase velocity C_0 in still water and C_a propagating against the drift current as a function of wave length L. Figure 10 shows the corresponding group velocities calculated by Eq. (42). In the present experiment the wave lengths are nearly 180 cm for the waves of period $T=1.111$ s and 100 cm for $T=0.833$ s. It can be seen from Fig. 9 that the phase speed is not so seriously affected by the existence of drift currents. The decrease of group velocity is at most 3% of that in still watar. Consequently, the effect of drift current on the phase and group velocities can be neglected for the present case of mechanically generated waves.

6.3 Wind Velocity Field

As previously stated in Section 2.2, the u component of the wind is 180° out of phase and the w component 90° forward with the motion of water surface. These characteristics are verified in Figs. 6 and 7.

The hot-films mounted on the wave-follower experience the vertical movement of the latter, so that correction must be made for the output signal from the anemometers.

The arrangement of the X-type film probe is illustrated in Fig. 11. In the figure U is the mean velocity in longitudinal direction, W the velocity induced by the motion of the wave follower, and u', v' and w' represent the turbulent motions in the x, y and z directions, respectively.

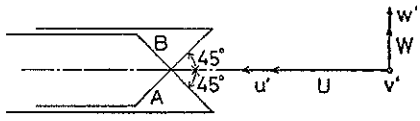

Fig. 11 X-Type Film Probe

The effective normal wind velocity $(U_{eff})_A$ for the film A is represented as

$$(U_{eff})_A=\left[\left\{\frac{1}{\sqrt{2}}(U+u')+\frac{1}{\sqrt{2}}(W+w')\right\}^2+v'^2\right]^{\frac{1}{2}},$$

$$\fallingdotseq\frac{1}{\sqrt{2}}(U+u'+W+w'), \tag{43}$$

correct to the first order. In the same way $(U_{eff})_B$ for the film B is

$$(U_{eff})_B\fallingdotseq\frac{1}{\sqrt{2}}(U+u'-W-w'). \tag{44}$$

Taking the time average of Eqs. (43) and (44), we get

$$(\bar{U}_{eff})_A=\frac{1}{\sqrt{2}}\bar{U}, \tag{45}$$

and

$$(\bar{U}_{eff})_B=\frac{1}{\sqrt{2}}\bar{U}. \tag{46}$$

Suppose that the output voltages from the linearizers which correspond to the film A and B are X and Y respectively, then the following relations can be obtained as

$$(\bar{U}_{eff})_A=\frac{1}{\sqrt{2}}\bar{U}=\frac{1}{\sqrt{2}}\xi\overline{X}, \tag{47}$$

and

$$(\bar{U}_{eff})_B=\frac{1}{\sqrt{2}}\bar{U}=\frac{1}{\sqrt{2}}\zeta\overline{Y}, \tag{48}$$

where ξ and ζ are constants which must be determined by calibration.

From Eqs. (43), (44), (47), and (48) the horizontal and vertical velocity components can be expressed as

$$U+u'=\frac{\xi}{2}X+\frac{\zeta}{2}Y, \tag{49}$$

$$W+w'=\frac{\xi}{2}X-\frac{\zeta}{2}Y, \tag{50}$$

where W can be calculated from the output signal of the wave-follower. In the wave following coordinate system, the measured vertical wind velocity was corrected by making use of Eq. (50).

The 'Reynolds stress' $\tau_{ij}=-\rho_a\overline{u_iu_j}$ is a symmetric second-order tensor. When $i=j$, the Reynolds stress τ_{ij} represents a normal stress which equals the negative of the static pressure (i.e. $\tau_{ij}=-p$) (*Young* 1983). When $i\neq j$, the Reynolds stress τ_{ij} represents a tangential stress. Both normal and tangential stress components cause an energy flux to (or from) the waves as explained in Section 2.3.

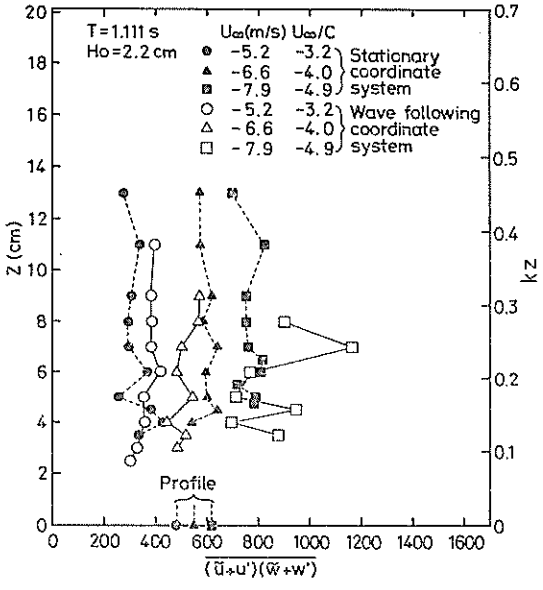

Fig. 12 Vertical Distribution of Reynolds Stress

Generally, the Reynolds stress is described without the density of the fluid. In this study, we also give an account of the Reynolds stress without ρ_a such as $-\overline{u_iu_j}$.

Measured values of the Reynolds stress are represented in Fig. 12 for both the stationary and wave following coordinate systems. In the case of $U_\infty=-5.2$ m/s, both coordinate systems give approximately the same Reynolds stress near the water surface. In the case of $U_\infty=-6.6$ m/s, the wave following coordinate system gives smaller Reynolds stress than the stationary coordinate system. When $U_\infty=-7.9$ m/s the data shows a large scatter for the wave following coordinate system. Except for this case the Reynolds stress is nearly constant over the height of measurement.

The values of the Reynolds stress estimated by the application of the logarithmic law to the mean wind velocity profiles are also plotted in Fig. 12 with the mark "Profile". In the case of $U_\infty=-6.6$ m/s, both methods give nearly the same value.

For other wind speeds, however, the profile method gives a smaller value than the direct measurement for $U_\infty=-7.9$ m/s and it does reverse for $U_\infty=-5.2$ m/s.

Chao and Hsu (1978) have shown in the experiment of the turbulent Reynolds stress over the progressive sinusoidal (1.0 Hz) water waves that the measurement of the Reynolds stress in the wave following coordinate system yields consistent results with those by the profile method. In this study the Reynolds stress obtained in the wave following coordinate system is extrapolated to the water surface to estimate its value there.

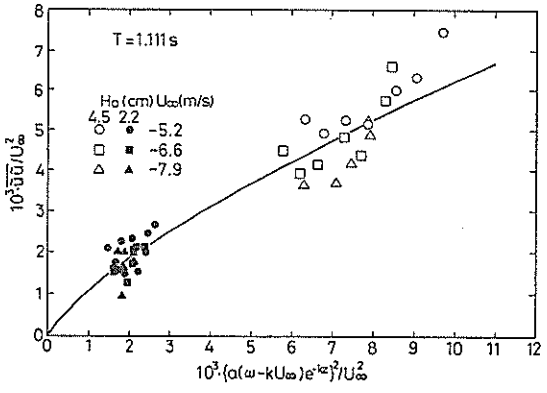

Fig. 13 Wave-Induced Reynolds Stress $\overline{\tilde{u}\tilde{u}}$

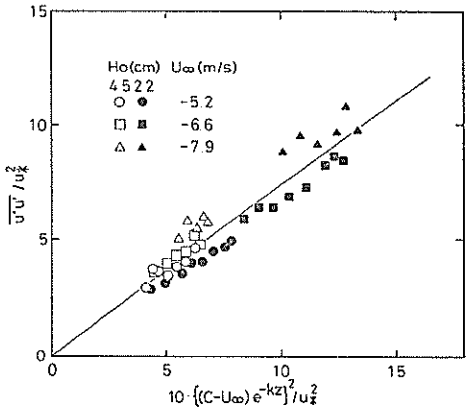

Fig. 14 Turbulent Reynolds Stress $\overline{u'u'}$

The normal component of the Reynolds stress is separated into two terms, nemely, $\overline{\tilde{u}\tilde{u}}$ and $\overline{u'u'}$. The wave-induced term $\overline{\tilde{u}\tilde{u}}$ is illustrated in Fig. 13. The solid curve represents the relation

$$\frac{\overline{\tilde{u}\tilde{u}}}{U_\infty^2}=0.0011\left[\frac{10^3}{U_\infty^2}\{a(\omega-kU_\infty)e^{-kz}\}^2\right]^{0.72} \tag{51}$$

Figure 14 shows the term $\overline{u'u'}$ and the straight line is given as

$$\frac{\overline{u'u'}}{u_*^2}=\frac{0.00734}{u_*^2}\{(C-U_\infty)e^{-kz}\}^2. \tag{52}$$

where u_* is that estimated by the profile method. Correlation between the wave-induced and turbulence components of wind ($\overline{\tilde{u}u'}$) was calculated, and it was confirmed that the correlation was negligibly small compared with the $\overline{\tilde{u}\tilde{u}}$ or $\overline{u'u'}$ term.

6.4 Surface Pressure Field

The phase difference between the static pressure and the water surface elevation is examined in Fig. 15. On account of the finite length of the vinyl chloride pipe connecting the disc probe with the pressure tranceducer, a certain amount of phase lag in the pressure is caused. The phase lag of the total pressure measuring system was carefully checked by using a specially designed pressure production system. The pressure transducer was attached to one end of an vacant acrylic cylinder with a reciprocating piston at the other end. The piston was activated by a crank-wheel system, which was driven by an induction motor with the variable rotational speed. By this system, cycric pressure variations with different frequencies and amplitudes were applied to the transducer.

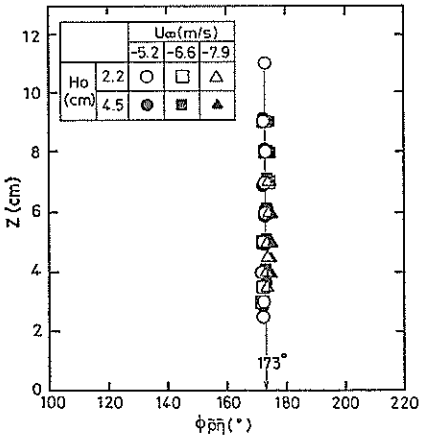

Fig. 15 Phase Difference between $\tilde{p}$ and $\tilde{\eta}$

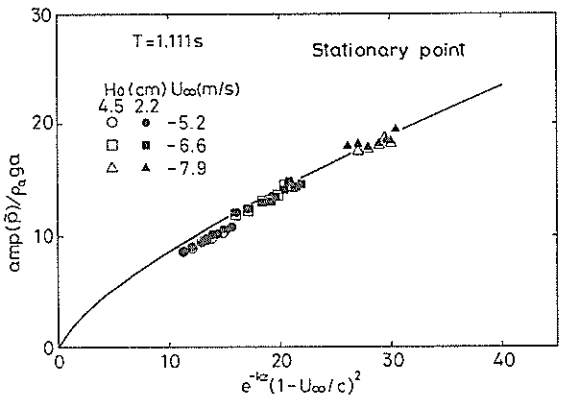

Fig. 16 Wave-Induced Pressure $\tilde{p}$ (wave following coordinate system)

The phase lag originated in the pipe ranged from 1.3° for the frequency $f=0.8$ Hz to 2.3° for $f=1.37$ Hz, and it was 1.5° for $f=0.9$ Hz which corresponds to the frequency of regular waves in this experiment.

The data plotted in Fig. 15 are those which have been corrected by the above-stated method. All the data show little scatter and yield the value 173° on the average.

Variation of the static pressure amplitude with respect to the elevation above the moving water surface is illustrated in Fig. 16. The solid curve has been estimated by the least-square method, and it can be expressed as

$$\frac{\mathrm{amp}(\tilde{p})}{\rho_a g a}=1.63\left\{e^{-kz}\left(1-\frac{U_\infty}{C}\right)^2\right\}^{0.72} \tag{53}$$

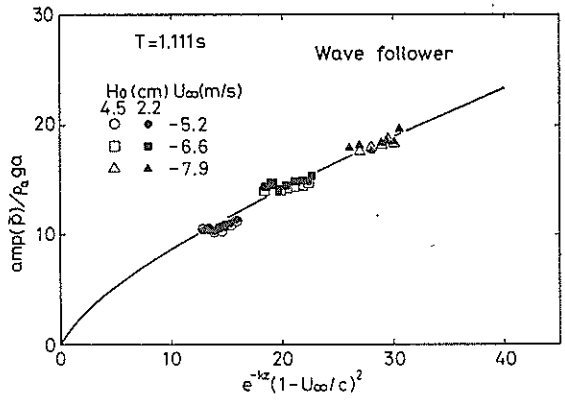

Fig. 17 Wave-Induced Pressure $\tilde{p}$ (stationary coordinate system)

Figure 17 shows the static pressure amplitude measured in the stationary coordinate system. The solid curve in Fig. 17 represents Eq (53). The difference between the wave-induced pressures in the stationary and wave following coordinate system is rather small.

6.5 Wind-Wave Energy Flux

The cross-spectrum between the static pressure $p(t)$ and surface elevation $\eta(t)$ is exprssed as

$$G_{p\eta}(f)=Co_{p\eta}(f)+iQ_{p\eta}(f), \tag{54}$$

where $Co_{p\eta}(f)$ is the co-spectrum, a real-valued even function of f, and $Q_{p\eta}(f)$ is the quadrature-spectrum, a real-valued odd function of f.

The energy flux from the wind to the waves caused by the pressure $p(t)$ on the waves is represented as

$$\frac{dE}{dt}=-p(t)\frac{\partial\eta(t)}{\partial t}. \tag{55}$$

If we take the Fourier transform on both sides of Eq. (55), then an energy flux spectrum can be obtained as

$$\dot{E}(f)=\omega Q_{p\eta}(f), \tag{56}$$

where the dot denotes the differentiation with respect to time. The mean rate of the energy flux $\overline{\dot{E}}$ from the wind to the waves is given by the relation

$$\overline{\dot{E}}=\int_0^\infty \dot{E}(f)df, \tag{57}$$

(see *Dobson* 1971).

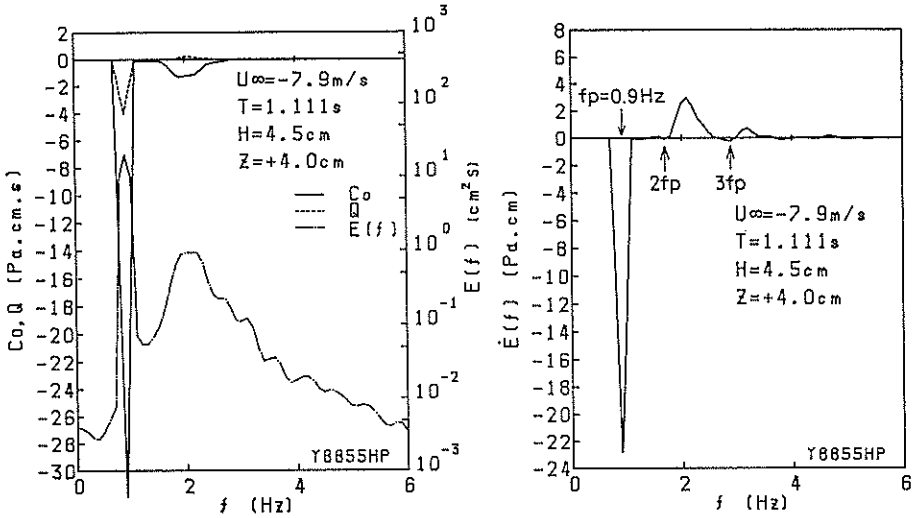

Fig. 18 Co- and Quadrature-Spectrum of Static Pressure and Surface Elevation, Auto Spectrum of Surface Elevation, and Dissipation Spectrum (Regular Waves f=0.9 Hz)

Figure 18 shows the co- and quadrature-spectrum between the static pressure $p(t)$ and the surface elevation $\eta(t)$, the spectrum $E(f)$ of the surface elevation, and the energy flux spectrum $\dot{E}(f)$ in the case that the regular waves of T=1.111 s are propagating against the wind. The right-hand side of Fig. 18 shows the energy flux spectrum. The negative value at the peak frequency f_p=0.9 Hz indicates that the waves do work against the wind. It means the transfer of energy from the waves to the wind and the resultant

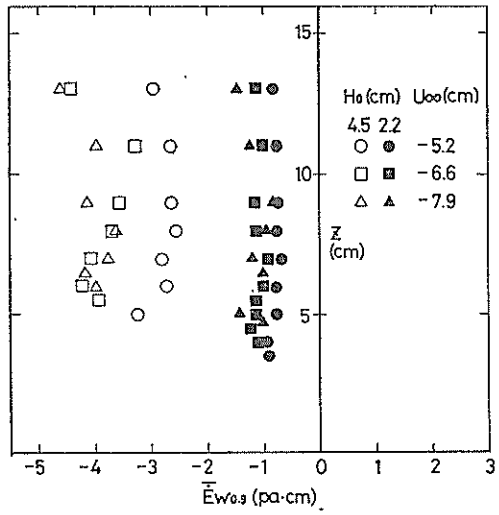

Fig. 19 Mean Rate of Energy Flux for the Wave Component

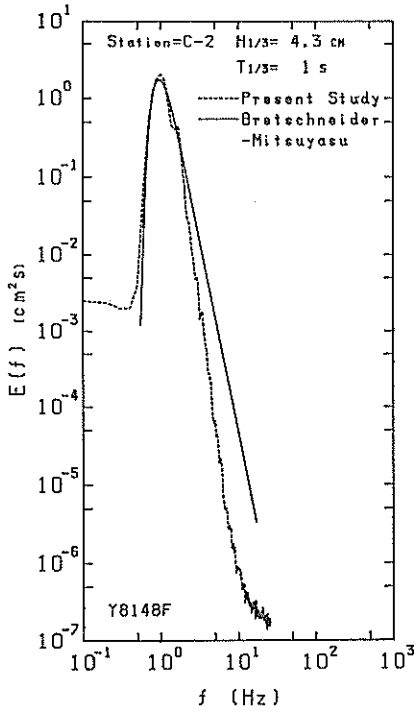

Fig. 21 Irregular Wave Spectra (Bretschneider-Mitsuyasu and Observed Spectrum)

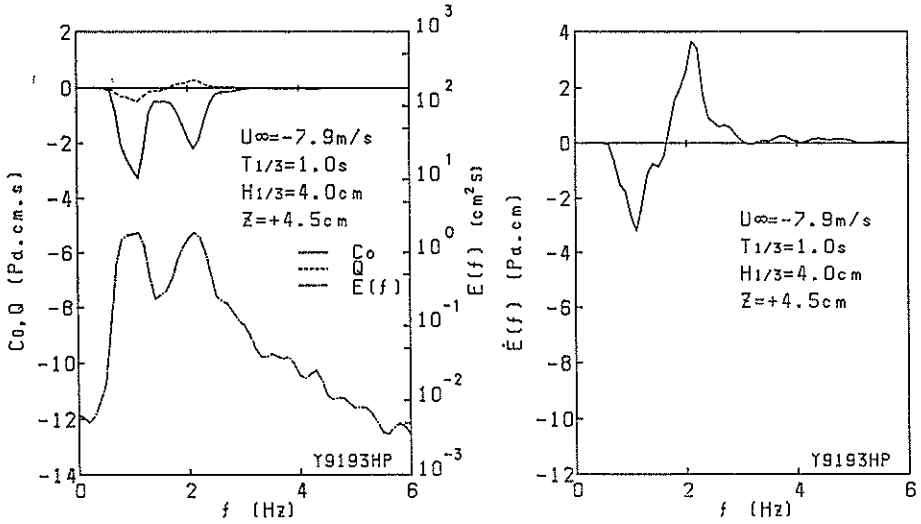

Fig. 20 Co- and Quadrature-Spectrum of Static Pressure and Surface Elevation, Auto Spectrum of Surface Elevation, and Dissipation Spectrum (Irregular Waves $T_{1/3}$=1.0 s)

attenuation of waves. At the harmonic frequencies $2f_p$ and $3f_p$, $\dot{E}(f)$ are also negative though the amount is small. Near the peak frequency of the wind waves, however, $\dot{E}(f)$ is positive. Figure 19 shows the mean rate of energy flux $\bar{\dot{E}}_{w0.9}$ for the peak frequency $f=0.9$ Hz of regular waves. It can be seen from Fig. 19 that as the wave height increases the energy flux from the waves to the wind increases.

An example of the spectra of irregular waves propagating against the wind is illustrated in Fig. 20. As in Fig. 18 the rate of energy flux for the dominant frequency components of irregular waves, is negative and it is positive for the wind-wave frequency components. The spectrum of irregular waves used here is shown in Fig. 21 which was measured in the absence of the wind. For comparison the Bretschneider-Mitsuyasu spectrum is also illustrated in Fig. 21. Examples of time series of the static pressure, turbulence components of the wind, and surface elevation in the case of irregular waves propagating against the wind are illustrated in Fig. 22.

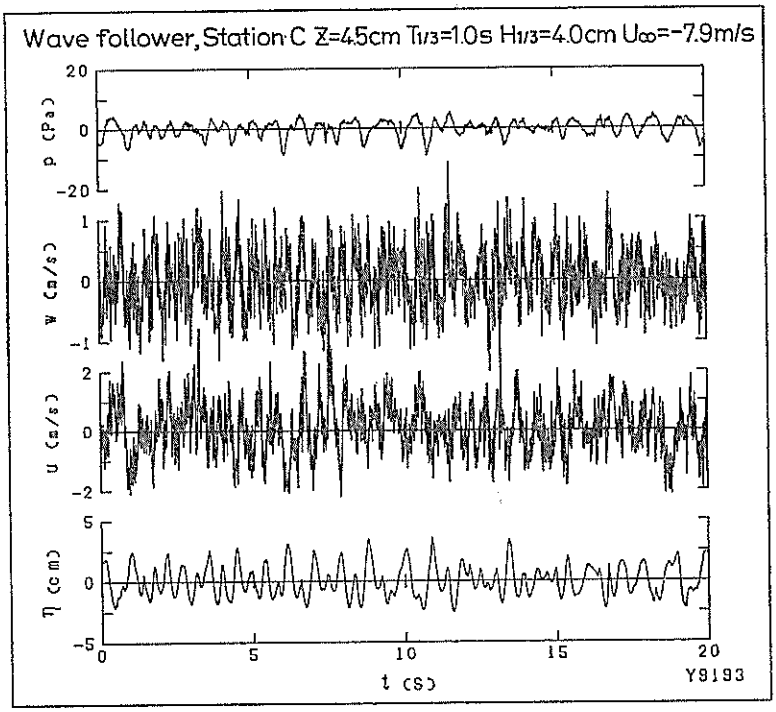

Fig. 22 Time Series of Surface Elevation η, Static pressure p, and Turbulence Components u and w (Irregular Waves $T_{1/3}=1.0$s, wave following coordinate system)

6.6 Estimation of the Coupling Coefficient

The coupling coefficient μ representing the air-water energy flux has been discussed in Section 2.3 and expressed by Eq. (26). The first term of Eq. (26) represents the contribution due to normal stress. The amplitude of the pressure component is expressed as Eq. (53). Substitution of Eq. (53) and the phase difference $\phi_{\bar{p}\bar{\eta}}=173°$ in the first term of Eq. (26) with $kz=0$ yields

$$\mu_1=-0.2\frac{\rho_a g}{\rho_w C^2 k}\left(1-\frac{U_\infty}{C}\right)^{1.44},$$

$$=-0.2\frac{\rho_a}{\rho_w}(\tanh kh)^{-1}\left(1-\frac{U_\infty}{C}\right)^{1.44}, \tag{58}$$

where μ_1 is the contribution of pressure to the coupling coefficient μ. In the above derivation, the relations of $C=\omega/k$ and $\omega^2=gk\tanh kh$ are utilized for generalization.

Strictly speaking, Eq. (26) for the coupling coefficient can be applied only to deep water waves. In this study, however, it is assumed that the effect of the finite depth appear only in the modification of the phase velocity. So that Eq. (58) can be regarded as an approximate expression of the coupling coefficient for finite depth area.

The second term in Eq. (26) represents the effect of the horizontal component of the Reynolds stress. By making use of Eqs. (51) and (52), the coupling coefficient due to the horizontal component of the Reynolds stress can be expressed as

$$\tilde{\mu}_2=-0.2\frac{\rho_a}{\rho_w}(ak)^{1.44}\left|\frac{U_\infty}{C}\right|^{0.56}\left(1-\frac{U_\infty}{C}\right)^{1.44}, \tag{59}$$

$$\mu_2'=-0.00734\frac{\rho_a}{\rho_w}\left(1-\frac{U_\infty}{C}\right)^2, \tag{60}$$

where $\tilde{\mu}_2$ and μ_2' are the contributions of the wave-induced and turbulent components of the horizontal Reynolds stress to the coupling coefficient μ.

Estimation of the contribution from the Reynolds stress $\overline{(\tilde{u}+u')(\tilde{w}+w')}$ has confirmed that this term is by one to two orders of magnitude smaller than the other two terms. Consequently, this term and contributions from the viscous stress are neglected in the estimation of μ.

The coupling coefficient μ_e is then represented as

$$\begin{aligned}\mu_e&=\mu_1+\tilde{\mu}_2+\mu_2'\\&=-0.2\frac{\rho_a}{\rho_w}\left(1-\frac{U_\infty}{C}\right)^{1.44}\left\{(\tanh kh)^{-1}+0.8(ak)^{1.44}\left|\frac{U_\infty}{C}\right|^{0.56}\right\}\\&\quad-0.00734\frac{\rho_a}{\rho_w}\left(1-\frac{U_\infty}{C}\right)^2,\end{aligned} \tag{61}$$

where μ_e represents the coupling coefficient estimated from the measured pressure and turbulence of the wind. Equation (61) shows that the coupling coefficient μ_e is a function of the wave slope ak, the ratio of the wind speed to the phase speed of the waves, and the relative depth kh. It can be seen from Eq. (61) that even in the case of no wave propagation, namely, $ak=0$, μ_e has some value. It would be natural that the coupling coefficient becomes zero if there are no waves. Therefore a correction factor for the coupling coefficient is introduced by taking into account the wave decay data. We consider that the correction factor D is the function of the relative wind speed U_∞/C and the wave slope ak. Moreover it should vary from zero to one according as ak varies from zero to some limiting value. Consequently, the correction factor D may be taken as

$$D=\tanh\left(-\gamma\frac{U_\infty}{C}ak\right), \tag{62}$$

where γ is a constant. By taking into consideration the wave decay data which will be described in detail in the next section, γ was estimated as 2.44 for $ak<0.2$.

Finally, the corrected coupling coefficient is expressed as

$$\mu=-\frac{\rho_a}{\rho_w}D\left[0.2\left(1-\frac{U_\infty}{C}\right)^{1.44}\left\{(\tanh kh)^{-1}+0.8(ak)^{1.44}\left|\frac{U_\infty}{C}\right|^{0.56}\right\}\right.$$

$$+0.00734\left(1-\frac{U_\infty}{C}\right)^2\Big], \tag{63}$$

$$\left.\begin{aligned} D&=\tanh\left(-2.44\frac{U_\infty}{C}ak\right), && ak\leqq 0.2,\\ D&=1, && ak>0.2. \end{aligned}\right\} \tag{64}$$

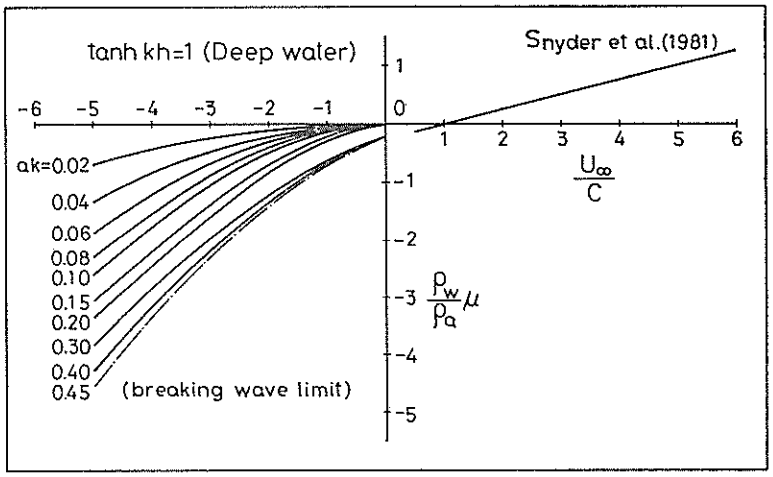

Fig. 23 Coupling Coefficient

Figure 23 shows the calculated result of Eq. (63) for various values of ak. In this figure the coupling coefficient for a following wind by *Snyder et al.* (1981) is also shown. The coupling coefficient in the case of an opposing wind which was estimated in this study, is smoothly connected to *Snyder's* relation. The discrepancy in the estimated coupling coefficient between $ak=0.2$ to 0.3 for lower wind speed may have been originated from the introduction of the correction factor D.

Young and Sobey (1985) have obtained a similar relation, but they neglected the contribution of the pressure. Their result gives smaller wave attenuation for $ak<0.4$ than that of the present study. Especially, the difference is remarkable for smaller value of ak.

6.7 Damping Coefficient of Mechanically Generated Waves

Water waves experience a certain degree of attenuation during propagation owing to the effects of adverse wind, viscous friction at the bottom and surface, etc. The decrease of wave height due to attenuation is usually expressed in the form of exponential decay such as

$$H=H_0\exp(-\alpha kx), \tag{65}$$

where H_0 and H are the initial and final wave heights, respectively, x the distance between the initial and final stations, and k the wave number. The factor α is called the damping coefficient.

If we consider the steady-state condition, the radiative energy transfer equation, Eq. (1) can be integrated with respect to x as

$$E=E_0\exp\left(\frac{\mu\omega}{C_g}x\right), \tag{66}$$

where E_0 and E are the initial and final power spectral densities of the component waves with the angular frequency ω.

From Eqs. (65) and (66), the damping coefficient α can be represented as

$$\alpha = -\frac{\mu C}{2C_g},$$

$$= -\frac{\mu}{2n}, \tag{67}$$

where

$$n = \frac{1}{2}\left(1 + \frac{2kh}{\sinh 2kh}\right). \tag{68}$$

Here the effect of the finite depth is provisionally adopted only in the ratio of the group velocity to the phase velocity.

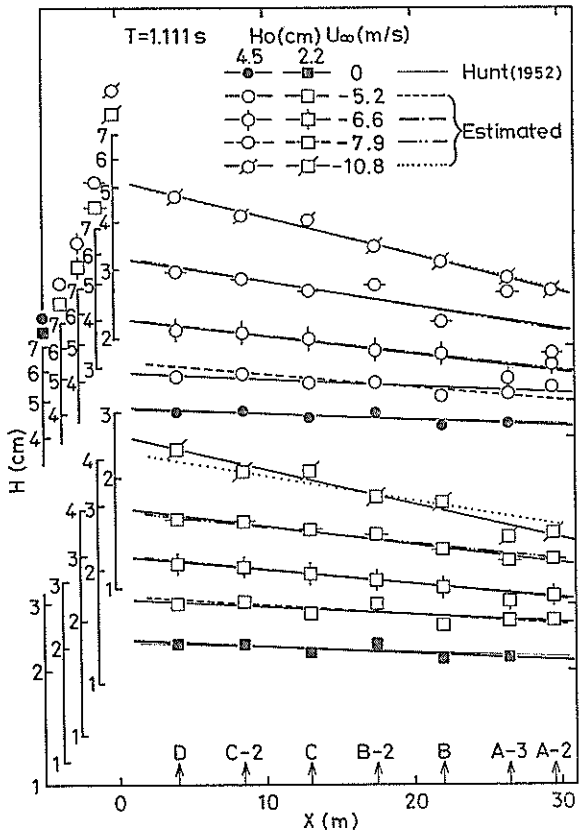

Fig. 24 Decay of Regular Waves with Fetch ($T=1.111$ s)

Figure 24 shows the damping of regular waves ($T=1.111$ s) with respect to the distance x. The thick solid lines are drawn by the least square method applied to the experimental data. Solid circles and squares are for the cases of no wind. In the latter case the viscous damping at the bottom and side walls which has been given by *Hunt* (1952) is calculad and drawn as thin solid lines. The theory and the experimental

data are in good agreement. If the viscous damping coefficient is defined as α_0, then Eq. (67) should be corrected for the term α_0 as

$$\alpha-\alpha_0=-\frac{\mu}{2n}. \tag{69}$$

In Fig. 24 the estimated values of wave damping using Eqs. (63) and (69) are also shown with straight lines (dashed, dotted, and dash-dots lines). The agreement is fairly good. Figure 25 shows the damping of regular waves with the period $T=0.833$ s. For higher wave height ($H_0=4.4$ cm) the difference between the observed and estimated data becomes noticeable especially for higher wind speeds. As a whole, however, it can be said that the coupling coefficient μ given by Eq. (63) can provide the reasonable estimate of the wave attenuation by the adverse wind.

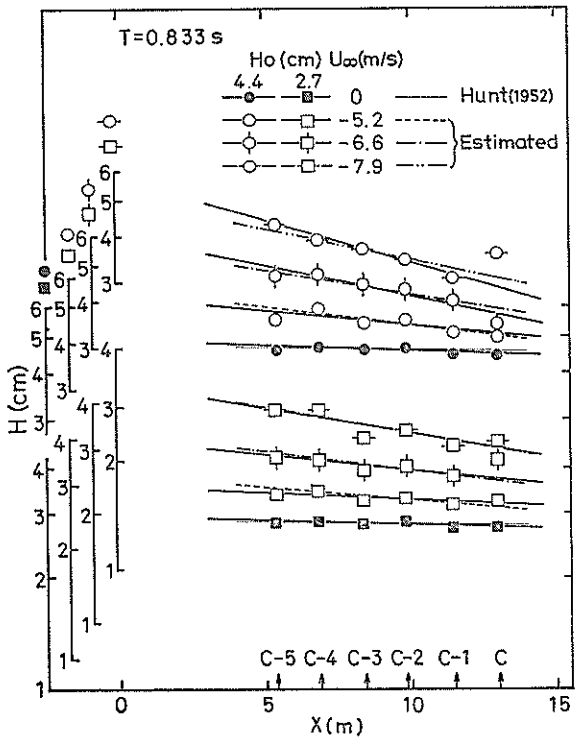

Fig. 25 Decay of Regular Waves with Fetch ($T=0.833$ s)

Figure 26 shows the demping of frequency components of irregular waves. In the case of irregular waves, spectral density $E(f)$ contains two components, i. e. one is that of the mechanically generated waves which propagate against the wind and another is that of the wind waves. In this study, it is assumed that the local generation of wind waves is not affected by the existence of the mechanically generated irregular waves. Consequently, spectral density $E(f)$ of the mechanically generated waves in an opposing wind can be obtained by subtracting the spectral density of pure wind waves which have been obtained by the experiment conducted in the wind only conditions from the composite component of the mechanically generated and wind waves. Several frequency components are chosen as representative component waves. The thin solid lines are estimated by applying the least square method to the measured data. Prediction of wave decay to this data

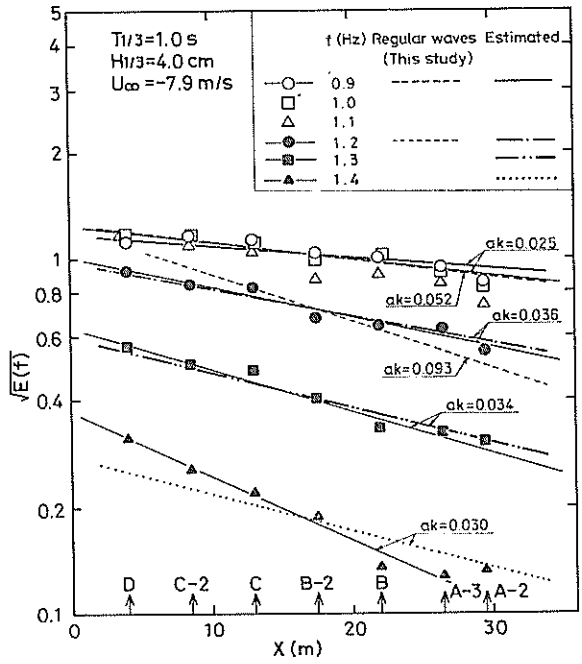

Fig. 26 Decay of Irregular Wave Components ($T_{1/3}$=1.0 s)

was made as follows. As the spectral density of the surface elevation $E(f)$ corresponds to the power of component waves, the square root of the spectral density $\sqrt{E(f)}$ should be proportional to the wave height of the component waves with the frequency f. The vertical axis in Fig. 26 is taken as $\sqrt{E(f)}$ which is a measure of the wave height. The wave amplitude a is calculated by the relation $a=\sqrt{2\overline{\eta^2}}=\sqrt{2E(f)\Delta f}$, where $\overline{\eta^2}$ is the mean-square value of the component waves. The wave number k is estimated by the wave length L of the component waves by the application of the small amplitude wave theory. For each component waves in Fig. 26, ak was estimated by the above mentioned method and the damping coefficient was calculated by Eqs. (63) and (69). The calculated damping of component waves is illustrated in Fig. 26 as 'Estimated' lines. The measured and estimated wave damping is not so different in the present experimental conditions especially near the dominant frequency. The damping of the regular waves are also shown in Fig. 26. The discrepancy between the damping of regular and component waves is mainly originated from the difference of the wave slope ak. It can be concluded from Fig. 26 that the component waves of irregular waves near the dominant frequency can be estimated by using Eq. (63).

7. Discussions

It can be easily seen from Eq. (67) that the damping coefficient α varies from $-\mu$ for deep water waves to $-\mu/2$ for long waves. Figure 27 and 28 present the diagrams of wave damping calculated from Eqs. (63) and (67) for the deep water area and the intermediate depth area with kh=1, respectively. Figure 29 shows the wave damping in the deep water for longer distance x. These figures represent the wave damping by an opposing wind only. Therefore, in using these figures, another damping sources such as bottom and internal friction must be considered, if necessary.

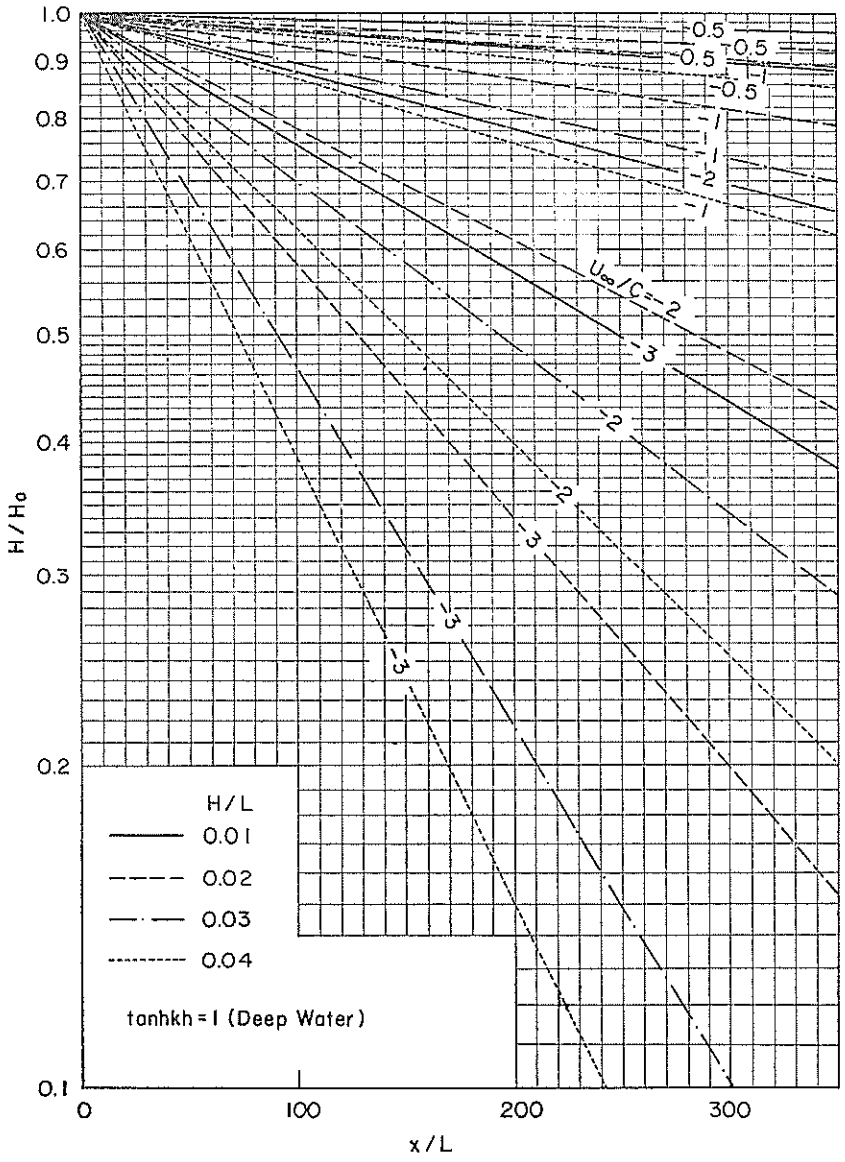

Fig. 27 Diagram of Wave Damping (Deep Water)

To show an example, we consider the decay of swell which is reflected by a breakwater and proceeding against the wind. Suppose that the wave period is 10 s and wind speed is 15 m/s or $U_\infty/C=-0.96$. For simplicity, it is also assumed that the water depth is deep enough so that the waves can be regarded as the deep water waves. Then, we can use Fig. 27 or 29. For the wave height $H=80$ cm, the wave slope H/L can be calculated as 0.005. At the distance $x=50$ km, the ratio of the distance to the wave length x/L becomes 320 and the ratio of the final wave hieght to the initial wave height H/H_0 can be read from Fig. 29 as 0.95. Consequently, the wave height becomes 76 cm at $x=50$ km.

Generally, swell with relatively small wave steepness can be regarded as long-crested waves and the above mentioned method can be thought as reasonable.

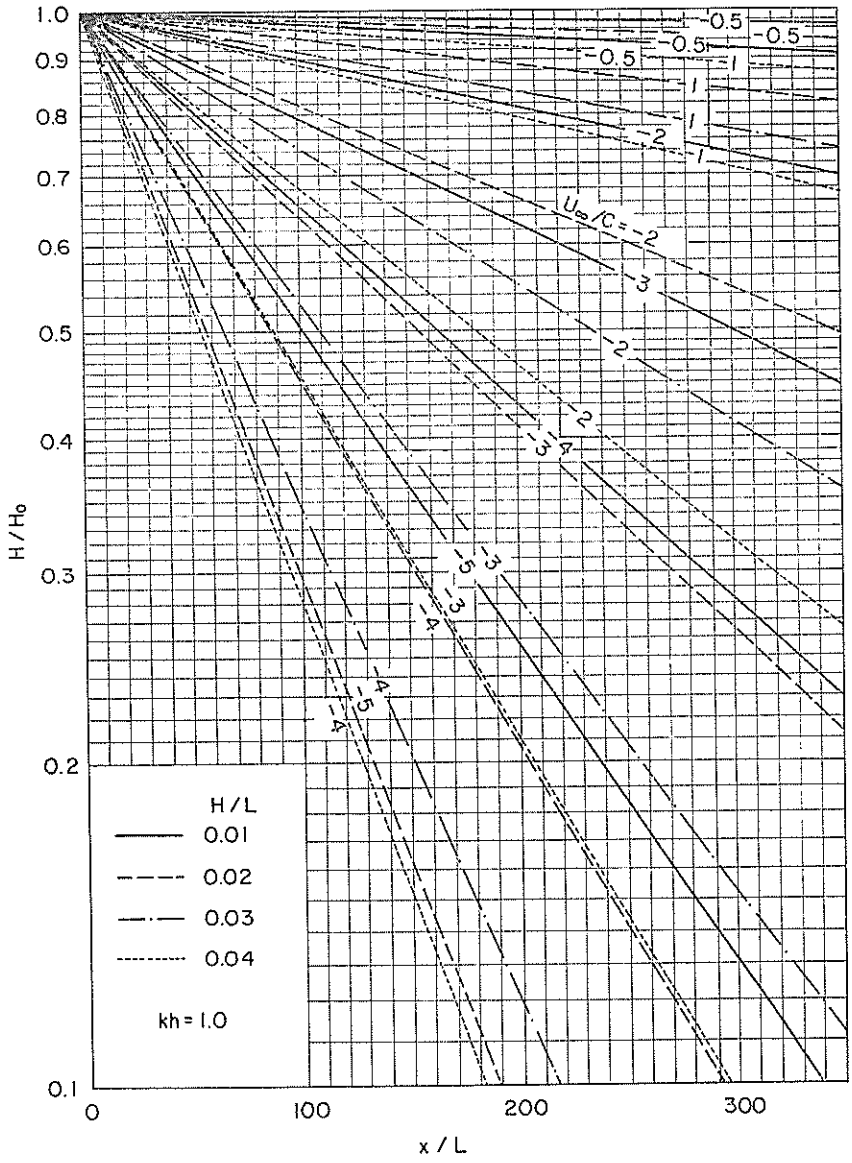

Fig. 28 Diagram of Wave Damping (kh=1, Shallow Water)

Wind waves, on the other hand, have the frequency spectrum of relatively wide frequency range and directional spreading. Both terms cause a decrease of wave height during the propagation of wind waves. These factors are not taken into account in the present study, and due consideration should be given in practical applications. Another example is given for the decay of short period wind waves. We consider a lake of which length is 20 km and the mean water depth is 4 m. The uniform wind with the speed 10 m/s is assumed to blow over the lake. The wind waves generated in a shallow lake can be estimated from the improved S-M-B method by *Ijima* (1968), namely,

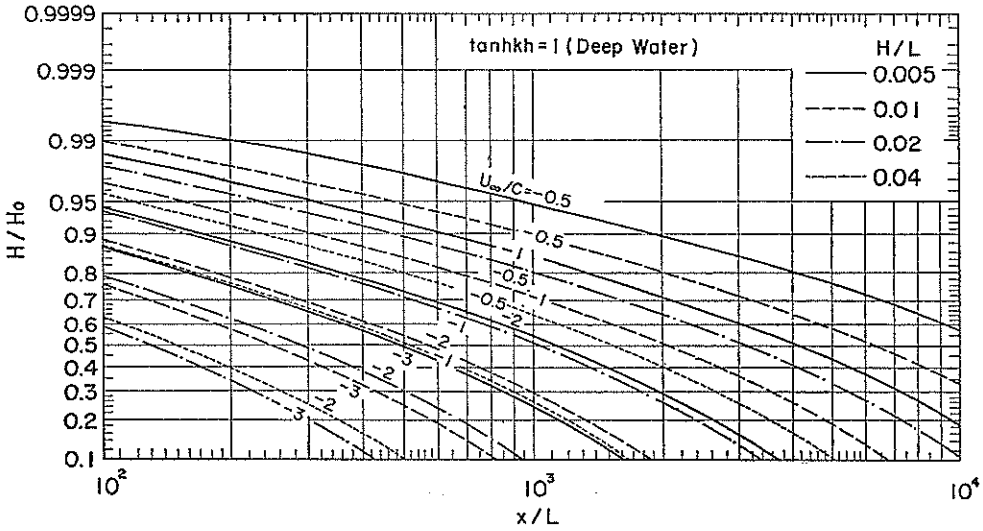

Fig. 29 Diagram of Wave Damping (Deep Water)

$$\frac{gH_{1/3}}{U_{10}^2}=0.30A\left[1-\left\{1+0.004\left(\frac{gF}{U_{10}^2}\right)^{\frac{1}{2}}/A\right\}^{-2}\right], \tag{70}$$

$$\frac{gT_{1/3}}{2\pi U_{10}}=1.37B\left[1-\left\{1+0.008\left(\frac{gF}{U_{10}^2}\right)^{\frac{1}{3}}/B\right\}^{-5}\right], \tag{71}$$

where

$$A=\tanh\left\{0.578\left(\frac{gh}{U_{10}^2}\right)^{\frac{3}{4}}\right\}, \tag{72}$$

$$B=\tanh\left\{0.520\left(\frac{gh}{U_{10}^2}\right)^{\frac{3}{8}}\right\}, \tag{73}$$

For the fetch 20 km, the wind speed U_{10} =10 m/s and the water depth 4 m, Eqs. (70) and (71) yield the estimates

$$H_{1/3}=0.53, \text{ (m)} \tag{74}$$

and

$$T_{1/3}=2.2. \text{ (s)} \tag{75}$$

For the wave period $T_{1/3}=2.2$ s, the wave length $L=7.53$ m. Then the wave slope becomes

$$\frac{H_0}{L}=0.07. \tag{76}$$

It is assumed that these wind waves are perfectly reflected by a vertical revetment at the shore and propagate against the wind which have generated them. The decrease of the height of reflected wind waves can be read off from Fig. 30 for several representative values of the distance x as in Table 2.

Next, the reduction of wave height by a bottom friction is considered. The ratio of wave height to the initial wave height is represented as

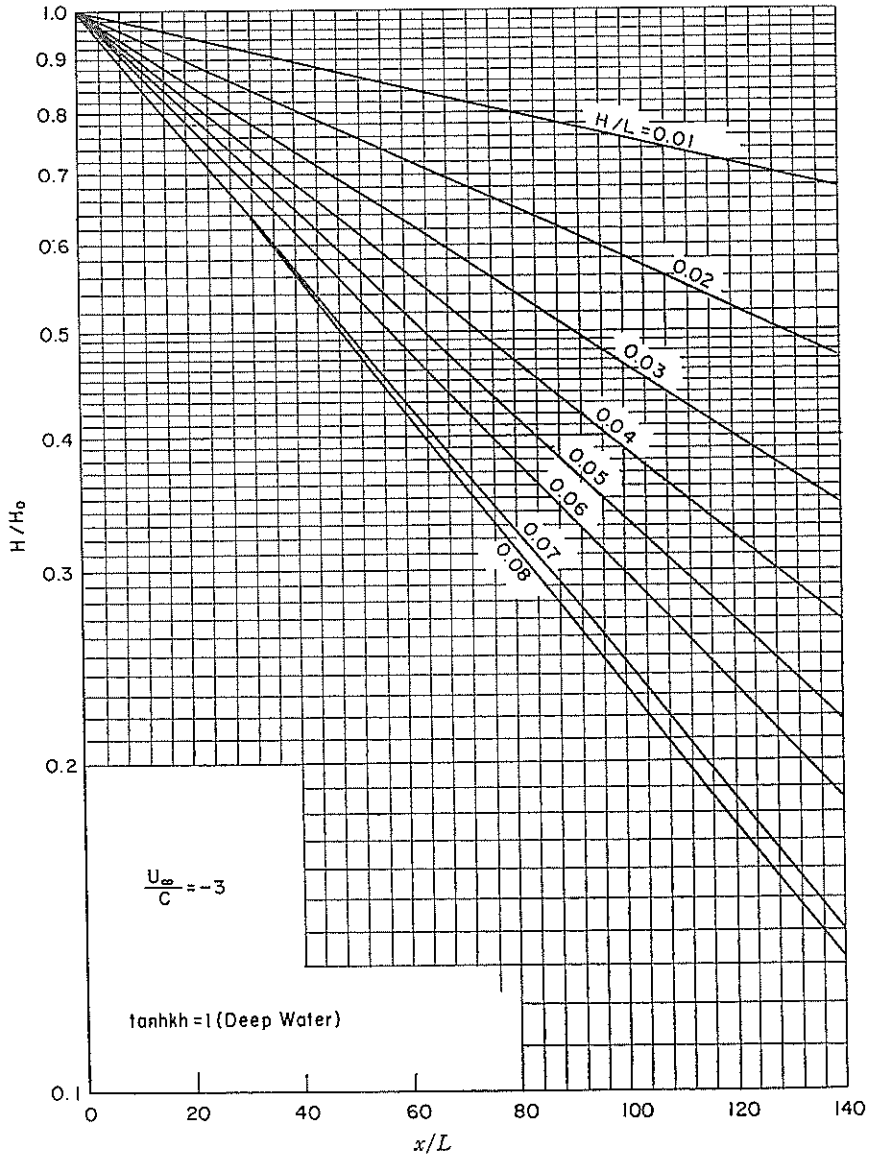

Fig. 30 Diagram of Wave Damping ($U_\infty/C=-3$, Deep Water)

Teble 2 Damping of Waves

	Adverse wind			Viscous damping		Turbulent damping	
				$f=0.0258$		$f=4$	
x (m)	$\frac{x}{L}$	$\frac{H}{H_0}$	H(m)	$\frac{H_v}{H_0}$	H_v(m)	$\frac{H_t}{H_0}$	H_t(m)
120	15.9	0.80	0.42	0.9998	0.53	0.974	0.52
240	31.9	0.64	0.34	0.9997	0.53	0.949	0.50
360	47.8	0.51	0.27	0.9995	0.53	0.926	0.49

$$\frac{H}{H_0}=\left[1+\frac{64}{3}\frac{\pi^3}{g^2}\frac{fH_0F}{h^2}\left(\frac{h}{T^2}\right)^2\frac{K_s^2}{\sinh^3(2\pi h/L)}\right]^{-1}, \tag{77}$$

where

$$K_s=\left[\left\{1+\frac{4\pi h/L}{\sinh(4\pi h/L)}\right\}\tanh\frac{2\pi h}{L}\right]^{-\frac{1}{2}} \tag{78}$$

is the shoaring factor and f the friction coefficient (see for example, *Hydraulic Formulas*, 1985).

For the viscous boundary layer, the friction coefficient can be represented as

$$f=2.08\,R_{eT}^{-1/2}, \tag{79}$$

where

$$R_{eT}=\frac{u_{b\max}^2T}{\nu_w}, \tag{80}$$

$u_{b\max}$ is the maximum longitudinal velocity at the bed, and ν_w the kinematic viscosity of water.

Iwagaki and Kakinuma (1966) has investigated the friction coefficient using the field data and obtained a diagram representing the relation between f and R_{eT}. It can be read from the diagram that the friction coefficient f is about two orders of magnitude larger than that obtained from Eq. (79).

In the above mentioned example for the lake, the Reynolds number R_{eT} is calculated and the value is

$$R_{eT}=6.46\times10^3. \tag{81}$$

The corresponding friction coefficient f in the field can be read from the diagram in *Iwagaki and Kimura* (1966) as

$$f\fallingdotseq4. \tag{82}$$

Damping of reflected waves by a viscous bottom friction H_v based on Eq. (79) and a turbulent bottom friction H_t based on Eq. (82) are also listed in Table 2. The damping by adverse wind is found to be much larger than that by viscous or turbulent damping at the bottom.

8. Conclusions

Experimental study on the wave decay in an opposing wind has been conducted in a large wind-wave tank.

A wave follower was used to measure the static pressure and turbulence components of wind at the constant elevations from the moving water surface. The coupling coefficient was estimated so that the wave decay in the experiment can be explained well.

The following results are summerized as follows:

1) The phase and group velocities were calculated where the wind-driven current exists. It was confirmed that the effect of wind-driven current on the phase and group velocities can be neglected for the present mechanically generated waves.
2) Wave-induced components for the static pressure and longitudinal Reynolds stress component of the wind and longitudinal turbulent Reynolds stress component of the wind were formulated. From these components coupling coefficient was estimated in terms of the wave slope and the ratio of wind speed to phase velocity of waves.
3) Correction factor for the coupling coefficient was estimated so that the damping coefficient of waves which are converted from the coupling coefficient can explain the

experimental decay of waves properly.

4) The diagrams of the wave decay in an opposing wind were presented in terms of the wave slope H/L and the relative wind speed U_∞/C.

(*Received on June 29, 1985*)

Acknowledgements

The authors wish to thank *Dr. Yoshimi Goda*, the Deputy Director General of the Port and Harbour Research Institute, for his suggestion to make diagrams of the wave decay in Chap. 7 and for his critical review of the manuscript. The authors also wish to express their thanks to *Dr. I. R. Young*, for his kindness to send us his doctoral thesis, which has contributed considerably to the completion of the present study.

References

1) BENDAT, J. S, and PIERSOL, A. G. (1966) : *Measurement and analysis of random data*, JOHN WILEY & SONS, Inc.
2) CHAO, S. P and HSU, E. Y. (1978) : Wave-induced velocities and turbulent Reynolds stresses above an air-water interface, *Dynamics of Atmospheres and Oceans*, Vol. 2, pp. 471–493.
3) DOBSON, F. W. (1971) : Measurements of atmospheric pressure on wind-generated sea waves, *Jour. Fluid Mech.*, Vol. 48, part 1, pp. 91–127.
4) ELLIOTT, J. A. (1972) : Microscale pressure fluctuations near waves being generated by wind, *Jour. Fluid Mech.*, Vol. 54, pp. 427–448.
5) HASSELMANN, K. (1963) : On the non-linear energy transfer in a gravity wave spectrum Part 2. Conservation theorems ; wave-particle analogy ; irreversibility, *Jour. Fluid Mech.*, Vol. 15, Part 2, pp. 273–281.
6) HASSELMANN, K. (1968) : *Basic Developments in Fluid Dynamics*, Vol. 2, M. Holt (Ed.), Academic Press, pp. 117–182.
7) HASSELMANN, K. and COLLINS, J. I. (1968) : Spectral dissipation of finite-depth gravity waves due to turbulent bottom friction, *Jour. Marine Res.*, Vol. 26, pp. 1–12.
8) HSU, C. T., HSU, E. Y. and STREET, R. L. (1981) : On the structure of turbulent flow over a progressive water wave : theory and experiment in a transformed wave-following co-ordinate system, *Jour. Fluid Mech.*, Vol. 105, pp. 87–117.
9) HSU, C. T. and HSU, E. Y. (1983) : On the structure of turbulent flow over a progressive water wave : theory and experiment in a transformed wave-following co-ordinate system. Part 2, *Jour. Fluid Mech.*, Vol. 131, pp. 123–153.
10) HUNT, J. W. (1952) : Viscous damping of waves over an inclined bed in a channel of finite width, *La Houille Blanche*, Vol. 7, pp. 836–842.
11) IJIMA, T. (1968) : See for example *Hydraulic Formulas (in Japanese)*, Japan Society of Civil Engineers, 625p.
12) IWAGAKI, Y. and KAKINUMA, T. (1966) : Field observation of the bottom friction factor in the coast (2) (*in Japanese*). *Proc. 13th Japan Conf. Coast. Eng.*, Japan Soc. Civil Eng., pp. 21–29.
13) JAPAN SOCIETY of CIVIL ENGINEERS (1985) : *Hydraulic Formulas (in Japanese)*, 625 p.
14) KATO, H. (1974) : Calculation of the wave speed for a logarithmic drift current, *Rept. Port and Harbour Res. Inst.*, Vol. 13, No. 4, pp. 3–32.
15) KATO, H., TSURUYA, H., DOI, T. and MIYAZAKI, Y. (1976) : Experimental study of wind waves generated on water currents (2nd Report) (*in Japanese*), *Rept. Port and Harbour Res. Inst.*, Vol. 15, pp. 3–48.
16) LAMB, H. (1932) : *Hydrodynamics*, 6th ed. Cambridge Univ. Press.
17) LONGUET-HIGGINS, M. S. (1969) : Action of a variable stress at the surface of water waves. *Physics of Fluids*, Vol. 12, No. 4, pp. 737–740.
18) MILES, J. W. (1957) : On the generation of surface waves by shear flows, *Jour. Fluid Mech.*, Vol. 3, pp. 185–204.

19) MITSUYASU, H. (1968) : On the growth of the spectrum of wind-generated waves (1), *Rept. Res. Inst. Appl. Mech.*, Vol. XVI, No. 55, pp. 459-482.
20) MITSUYASU, H. and MIZUNO, S. (1971) : Experimental study on the wave decay under an adverse wind (*in Japanese*), *Proc. 18th Japan Conf. Coast. Eng.*, Japan Soc. Civil Eng., pp. 37-42.
21) MITSUYASU, H. and RIKIISHI, K. (1978) : The growth of duration-limited wind waves, *Jour. Fluid Mech.*, Vol. 85, part 4, pp.705-730.
22) MITSUYASU, H. and HONDA, T. (1982) : Wind-induced growth of water waves, *Jour. Fluid Mech.*, Vol. 123, pp. 425-442.
23) MIZUNO, S. and MITSUYASU, H. (1973) : Effects of adverse wind on the phase velocity of mechanically generated waves, *Rept. Res. Inst. Appl. Mech.*, Vol. XXI, No. 68, pp. 33-52.
24) MIZUNO, S. (1975) : Growth of mechanically generated waves under a following wind, I. *Rept. Res. Inst. Appl. Mech.*, Vol. XXII, No. 71, 1975.
25) MIZUNO, S. (1976 a) : Turbulence measurements above mechanically generated water waves (*in Japanese*), *Bulletin Res. Inst. Appl. Mech.*, No. 45. pp. 451-471.
26) MIZUNO, S. (1976 b) : Pressure measurements above mechanically generated water waves (I) : *Rept. Res. Inst. Appl. Mech.*, Vol. XXIII, No. 75, pp. 113-129.
2) MIZUNO, S. (1978) : Turbulence measurements above mechanically generated waves (II) (*in Japanese*). *Bulletin Res. Inst. Appl. Mech.*, No. 48, pp. 39-60.
28) PHILLIPS, O. M. (1957) : On the generation of surface waves by turbulent wind, *Jour. Fluid. Mech.*, Vol. 2, pp. 417-445.
29) PLANT, W. J. (1982) : A relationship between wind stress and wave slope, *Jour. Geophys. Res.*, Vol. 87, No. C 3, pp. 1961-1967.
30) SHEMDIN, O. H. and HSU, E. Y. (1967) : Direct measurement of aerodynamic pressure above a simple progressive gravity wave, *Jour. Fluid Mech.*, Vol. 30, part 2, pp. 403-416.
31) SNYDER, R. L. (1974) : A field study of wave-induced pressure fluctuations above surface gravity waves, *Jour. Marine Res.*, Vol. 32, pp. 485-496.
32) SNYDER, R. L., DOBSON, F. W., ELLIOTT, J. A. and LONG, R. B.(1981) : Array measurements of atmospheric pressure fluctuations above surface gravity waves, *Jour. Fluid Mech.*, Vol. 102, pp. 1-50.
33) STEWART, R. H. and TEAGUE, C. (1980) : Dekameter radar observations of ocean wave growth and decay., *Jour. Phys. Oceanogr.*, Vol. 10, pp. 128-143.
34) WILSON, W. S., BANNER, M. L., FLOWER, R. J., MICHAEL, J. A. and WILSON, D. G. (1973) : Wind-induced growth of mechanically generated water waves, *Jour. Fluid Mech.*, Vol. 58, part 3, pp. 435-460.
35) YOUNG, I. R. (1983) : *The response of waves to an opposing wind*, Doctral thesis presented to James Cook University, 289 p.
36) YOUNG, I. R. and SOBEY, R. J. (1985) : Measurements of the wind-wave energy flux in an opposing wind, *Jour. Fluid Mech.*, Vol. 154, pp. 427-442.

List of Notations

A_n : wave amplitude for the n-th wave component
a : amplitude of waves
b : constant in the logarithmic distribution of wind drift current cf. Eq. (34)
C : phase velocity of waves
C_g : group velocity of waves
$Co_{p\eta}(f)$: co-spectrum between the static pressure $p(t)$ and surface elevation $\eta(t)$
C_0 : phase velocity of waves in still water
C_1, C_2 : first and second-order wave speeds, cf. Eq. (35)
D : correction factor for coupling coefficient μ
$E(f, \theta)$: directional spectral energy density of the component with the frequency f propagating toward the direction θ
$\dot{E}(f)$: energy flux spectrum

$\overline{\dot{E}}$: mean rate of energy flux
$\dot{E}_{w0\cdot9}$: mean rate of energy flux for the peak frequency $f=0.9$ Hz
E_0 : initial power spectral density
F : fetch
$F(k)$: energy spectrum in terms of wave number k
f : frequency
f_p : peak frequency of wave spectrum
f_1 : fundamental frequency
$G_{p\eta}(f)$: cross-spectrum between the static pressure $p(t)$ and surface elevation $\eta(t)$
g : acceleration of gravity
$g(t)$: instantaneous signal
$\overline{g}$: time average of $g(t)$
$\tilde{g}(t)$: wave induced quantity
$g'(t)$: turbulence component
H : wave height
H_0 : initial wave height
h : depth of water
K : constant for disc-type static pressure probe
k : wave number $(2\pi/L)$
L : wave length
N : total number of data used in a computation
p : pressure of air
p_d : pressure measured by disc probe
p_s : static pressure
$\overline{p}$: overall time avarage of pressure
$\tilde{p}$: wave-induced pressure
p' : turbulent residual of pressure
Q : cf. Eq. (37)
$Q_{p\eta}$: quadrature-spectrum between $p(t)$ anp $\eta(t)$
S : source function
s_a : air-sea interaction source term
s_d : dissipation source term
s_n : nonlinear wave-wave interaction source term
T : wave period
T_E : time that the wave energy reaches the inlet of wind
t : time
$(U_{eff})_A$: effective normal wind velocity for film A
$(U_{eff})_B$: effective normal wind velocity for film B
U_T : constant in the logarithmic distribution of wind drift current cf. Eq. (34)
U_w : horizontal component of wind drift current
U_{*a} : friction velocity of air
U_∞ : free-stream wind velocity
u : horizontal velocity
u_0 : surface velocity
$\tilde{u}$: wave-induced horizontal velocity
u' : horizontal turbulence velocity
W : vertical velocity induced by the movement of wave-follower
w : vertical velocity
X : output voltage from film A
x : horizontal cartesian coordinate
Y : output voltage from film B
y_1, y_2 : cf. Eqs. (39) and (40)
z : vertical cartesian coordinate
z_0 : roughness height
α : damping coefficient of waves

α_a : cf. Eq. (4)
α_0 : viscous damping coefficient
β_a : cf. Eq. (5)
γ : cf. Eq. (62)
Δt : data sampling time interval
δ : cf. Eq. (38)
ε : perturbation parameter ($=u_0/C_0$)
ζ : cf. Eq. (48)
θ : direction of wave propagation
μ : coupling coefficient
μ_a : dynamic viscosity of air
μ_e : coupling coefficient estimated from the measured pressure and turbulence of wind
ν : coupling coefficient
ν_w : kinematic viscosity of water
ξ : cf. Eq. (47)
Π : wave number-frequency spectrum of turbulent atmospheric pressure at the water surface
ρ_a : density of air
ρ_w : density of water
$\tilde{\sigma}_e$: effective normal stress
σ_{ij} : instantaneous stress tensor
ϕ : velocity potential
$\phi_{\tilde{p}\tilde{\eta}}$: phase difference between $\tilde{p}$ and $\tilde{\eta}$
ϕ_1 : velocity potential by wave perturbation
ω : angular frequency